

Life cycle of a mesoscale circular gust front observed by a C-band Doppler radar in West Africa

Marie Lothon ^{*(1)},

Bernard Campistron⁽¹⁾, Michel Chong⁽¹⁾,

Fleur Couvreur⁽²⁾, Françoise Guichard⁽²⁾, Catherine Rio⁽²⁾,

and Earle Williams⁽³⁾

(1) LABORATOIRE D'AÉROLOGIE, UNIVERSITÉ DE TOULOUSE, CNRS, TOULOUSE, FRANCE

(2) MÉTÉO-FRANCE, CNRM/GAME/GMME/MOANA, CNRS, TOULOUSE, FRANCE

(3) DEPT. OF CIVIL & ENVIRONMENTAL ENGINEERING, MASSACHUSETTS INSTITUTE OF TECHNOLOGY, CAMBRIDGE, MA, USA

** Corresponding author address:* Marie Lothon, Laboratoire d'Aérodynamique, Centre de Recherches Atmosphériques, 8 route de Lannemezan, 65300 Campistrous, France.

E-mail: marie.lothon@aero.obs-mip.fr

ABSTRACT

On 10 July 2006, during the Special Observation Period (SOP) of the African Monsoon Multidisciplinary Analysis (AMMA) campaign, a small convective system initiated over Niamey and propagated westward in the vicinity of several instruments activated in the area, including the Massachusetts Institute Technology (MIT) C-Band Doppler radar and the Atmospheric Radiation Measurement (ARM) mobile Facility. The system started after a typical convective development of the planetary boundary layer (PBL). It grew and propagated within the scope of the radar range, so that its entire life cycle is documented, from the precluding shallow convection to its traveling gust front. The analysis of the observations during the transitions from organized dry convection to shallow convection and from shallow convection to deep convection lends support to the significant role played by surface temperature heterogeneities and boundary-layer processes in the initiation of deep convection in semi-arid conditions. The analysis of the system later in the day, its growth and propagation, and its associated density current allows us to estimate the wake available potential energy and demonstrate its capability to trigger deep convection itself. Given the quality and density of observations related to this case, and its typical and quasi-textbook characteristics, we consider this a prime case for the study of deep convection initiation and evolution, and for testing their parameterizations in single column models.

1. Introduction

The deep convective systems that occur in West Africa during the boreal summer are often associated with African Easterly Waves (AEW; Thorncroft, 1995), which are known to play a significant role in deep convection in this region (Fink and Reiner, 2003; Lavaysse et al., 2006). The AEWs contribute to modulate the convective systems (Reed et al., 1977; Mathon et al., 2002), and are also found to initiate most Atlantic tropical cyclones downstream (Chen et al. 2000). But the convective systems can also be triggered locally as a result of surface heterogeneity—such as topography, moisture or temperature variability (Comer et al., 2007)—, or by mid-level propagating mesoscale dynamical disturbances generated by other convective systems or fronts. Over the land surface of West Africa, with substantial surface heating leading to deep boundary layers in the Sahel, and the presence of various heterogeneities and boundaries, several local or mesoscale processes other than gravity waves can contribute to the initiation of deep convection.

Weckwerth and Parsons (2006) carried out a review of convective initiation processes based on the IHOP-2002 experiment (Weckwerth et al. 2004), focusing predominantly on triggering by boundaries: frontal zones, drylines, gust fronts, boundary-layer rolls, bores and land surface effects. They observe that the boundary-layer convergence is often a precursor to deep convection, and that deep convection is sensitive to the strength of this convergence, the shear, and the spatial variability and amount of moisture, within this boundary (see also

previous studies such as Cooper et al., 1982). This is supported, for example, by the study of Weckwerth et al. (2008), who analyzed the extensive observations of deep convective cells occurring over one day of IHOP. The set of preconvective features include: a mesoscale low pressure region, a dryline and interacting old outflow boundary, internal gravity waves and horizontal convective rolls. Wilson et al. (1992) showed how the intersection of convective horizontal rolls with a convergence line can initiate intense thunderstorms. Kalthoff et al. (2009) also made a recent case study of the triggering effect of convergence zones. During IHOP_2002, Wilson and Roberts (2006) found the deep convection triggering sources evenly divided between surface-based convergence lines (occurring mostly in the afternoon or evening) and elevated episodes with no surface convergence (mostly at night). Finally, density currents generated by deep convective systems can themselves trigger new systems. Lifting potential of density currents associated was studied e. g. by Moncrieff and Liu (1999), in conjunction with the associated convergence, shear and dynamical organization. Lima and Wilson (2007) found that the lifting by gust fronts is the most common initiation process in the moist tropical environment of Amazonia (36 % of cases).

In the specific case of the Sahel region, when the wet season starts and the first rains are building wet patterns on the surface, surface moisture and temperature heterogeneities are a key to deep convection initiation (Alonge et al. 2007). The significance of boundary layer convergence in the Sahel is highlighted by Taylor et al. (2003). Taylor et al. (2007) suggest a significant role played by mesoscale convergence lines forced by soil moisture. Later, and based on a case study of

the African Monsoon Multidisciplinary Analysis (AMMA), Taylor et al. (2010) give further insight in this issue, showing the importance of dry/wet warm/cold boundaries in enhancing the chance of deep convection triggering with low-level convergence.

The 10 July 2006 case considered here allows us to address the distinct convective initiation mechanisms encountered in the Sahel. The substantial heating of the surface, which shows a pronounced meridional gradient in vegetation and soil moisture close to this region, the presence of the inter-tropical discontinuity (ITD) between the northeasterly dry Saharan air and the south-westerly moist monsoon flow (Fig. 1), and the presence of mountain massifs in Sahara are all likely to contribute to the occurrence of convergence lines or other triggering processes quoted previously. During the early stage of the monsoon considered here, the large-scale environment becomes more favorable to deep convection. However, smaller scale processes may also play a crucial role in convective initiation within this still moisture-limited context, especially at the beginning of the season. The storm system— henceforth S_0 —that is described hereafter grew and propagated within the scope of the radar, so that a large part of its life cycle is documented, from the preceding boundary-layer structure to the propagation of the cell and associated gust front. Our objective is to thoroughly study the different steps from the preceding dry convection to the gust front propagation, in order to better understand the factors which are involved in the initiation of the deep convection in those semi-arid conditions.

After presenting the experimental dataset and methodologies in Section 2, we

provide the context of the observations, describe the boundary-layer growth and structure prior to the development of the storm system and discuss the initiation of deep convection (Section 3). Section 4 describes the afternoon deep convection with an analysis of the density current (DC) and gust front.

2. Experimental dataset

The case studied here was revealed by the thorough 3D continuous scans of the MIT radar installed at Niamey airport, in Niger. The radar observations are complemented with radiosoundings, surface stations and wind profiler data, which were all colocated on the Atmospheric Radiation Measurement (ARM) mobile facility site, 1.6 km away from the MIT radar. Figure 2 locates the area of interest in Niger (Fig. 2a) and gives the topography around Niamey (Fig. 2b). We also used satellite observations.

a. The MIT C-band Doppler radar (13.49 °N, 2.17 °E)

The MIT radar is a 5.37-cm wavelength Doppler radar, with a 250 m pulse width and a 1.4° beamwidth. During AMMA, the MIT radar was operated continuously from July to September with scans based on a ten-min cycle. The scanning procedure in each 10-min cycle was composed of a long range (250 km) survey azimuthal scan at a low elevation (0.7°), followed by a volume scan at 15 elevation angles from 0.5° to 29.2° and a maximum range of 150 km. The

azimuthal and radial resolutions of the volume scans were of 1° and 250 m, respectively, while the Nyquist velocity was of 12.75 m s^{-1} . Optional RHI (range height indicator) scans were then performed at a chosen azimuth, depending on the area of interest. In this study, the volume scan data are analyzed either to provide a view of the horizontal and vertical organization of the radar reflectivity and/or Doppler velocity in clear and cloudy air, and possibly infer the 3D airflow structure associated with the convective system.

Reflectivity and Doppler velocity (corrected for velocity aliasing) data are interpolated onto a 3D Cartesian grid by using a Cressman (1959) weighting function depending on the distance between a grid point and the observed data point within an ellipsoid of influence centered on grid point and defined by its horizontal and vertical radii R_{xy} and R_z , respectively. Because the weighted mean acts as a spatial filter, these parameters are often the result of a compromise between expected resolved scales and sufficient data within the volume of influence. Because of the limited extension of elevation angles (about 30°), limitation of such weighting process occurs immediately above the radar site. (As a consequence, at 600 m height for example, data shown within 1 k m distance of the radar will come from this interpolation as soon as they are in a location affected by the volume of influence of an actual observation; otherwise, there will be no interpolated field data in this region. See Figs. 6 and 11 discussed later in the text.) Also, the divergence of the beams requires the use of a coarser resolution in the mid-troposphere for an optimized description of the structure.

Derivation of the 3D wind field from the MIT single-Doppler radar data is

based on the version of the multiple-Doppler synthesis and continuity adjustment technique (MUSCAT, Bousquet and Chong, 1998) adapted to ground-based radars (Chong and Bousquet, 2001). MUSCAT yields a simultaneous solution of the three wind components from at least two Doppler observations. In this context, single-radar data at two or more observation times can be assimilated as pseudo dual- or multiple-radar observations as long as temporal variations of the airflow and precipitation structures are dominated by advective processes. This is accomplished by considering a reference frame moving in tandem with the system with respect to a time of reference, as demonstrated by Chong (2010).

Even if rigorously accurate 3D wind structure is impossible to obtain with only one Doppler radar (Elía and Zawadzki 1997), this method allows us to retrieve an approximation of the motion inside the system through the use of three consecutive scans. As will be shown in Section 4, it is necessary to accommodate the fitting process by considering a varying grid resolution between observation times in order to take into account the expansive nature of the convection cell.

b. The ARM Facility instruments (13.48 °N, 2.17 °E)

The ARM Mobile Facility was deployed in Niamey near the airport, 1600 m from the MIT C-band radar nearly to the south (170°) of it. This allowed us to use the complementary information provided by a UHF wind profiler, a meteorological surface station, and four radiosoundings launched that day at 0530, 1130, 1730 and 2300 UTC, with a 10-m vertical resolution. (Note that

UTC = LT - 1.)

The ARM UHF wind profiler operates at 915 MHz wavelength. It detects backscattered signals from turbulence-induced atmospheric refractive index fluctuations at a scale of half the radar wavelength, transported by the flow (Balsley and Gage 1982). Thus the radar reflectivity is related to the structure parameter of the turbulence refractive index fluctuations C_n^2 (Gossard et al. 1982) defined in the inertial subrange. A sudden increase of C_n^2 with height is usually associated with sharp changes in atmospheric temperature and humidity under turbulence mixing, so that C_n^2 can be used to estimate the boundary-layer depth Z_i (Doviak and Zrnić, 1993; Angevine et al., 1994; Jacoby-Koaly et al., 2002). This profiler can also work in precipitation conditions but the scattering mechanism associated with precipitation echo is different from the clear air echo. These two types of echo cannot easily be separated in the UHF band. In rainfall, UHF radars are more sensitive to the precipitation echo, which masks the clear air echo.

For this profiler, the power is emitted in five beams successively, which in clear air allow the measurement of the three components of the wind, assuming local horizontal homogeneity of the wind field. In precipitation, the measured vertical velocity will mainly reflect the hydrometeor fall velocity. The vertical resolution of this profiler is 60 m in ‘low mode’ and 210 m in ‘high mode’. More information and technical details can be found in Kalapureddy et al. (2009).

c. Satellite dataset

We also use the Meteosat Second Generation (MSG) satellite data (from METEOSAT-8 onwards), and especially the images produced by the SEVIRI sensor (Aminou 2002), which represent the received radiation from the Earth and its atmosphere on 12 spectral channels, and are able to map the land surface temperature—which is the radiative skin temperature of the land surface—at 5-km horizontal resolution and every 15 min (Trigo et al. 2008).

Finally, we use the mapping of surface soil moisture retrieved from the AMSR-E observations and a rainfall Estimation of Precipitation by SATellite (EPSAT) product (Pellarin et al. 2009).

3. Context and preceding conditions

a. Large scale context

At this time of year, the monsoon flow is setting over West Africa, with the ongoing northward motion of the Intertropical convergence zone (ITCZ) (Sultan et al. 2007). Since early May in 2006, the monsoon southwesterly wind is set in Niamey (Lothon et al. 2008), replacing the Harmattan northeasterly wind of the dry season. The interface at the ground, the ITD, is situated a few hundred km north of Niamey latitude. The ITCZ is still centered around the coast of the Guinean Gulf.

Figure 1 shows the temperature at 950 hPa over West Africa on 10 July

2006, given by European Center for Medium-range Weather Forecasts (ECMWF) analyses, with the ITD, and mean sea level pressure field. One possible definition of the ITD is to consider the line of constant dew point temperature at 2 m a. g. l (Lothon et al. 2008). The large scale pressure field is characterized by a thermal low in the Sahara (called the Saharan heat low), which influences the penetration of the monsoon into the continent.

Niamey is situated in the Sahel region, which is a transition zone between the vegetated area to the south and the desert to the north. It is influenced by both the monsoon flow which brings humidity in the low levels and the dry Saharan Air Layer (SAL) above. When the ITD has crossed this region and the ITCZ is not far south, deep convection starts to occur in Sahel. 10 July 2006 is situated a few days before the so-called monsoon onset (Janicot and Sultan 2007), that is during a transition period at the beginning of the wet season, when deep convection is not plainly settled yet.

b. Convective boundary-layer growth in semi-arid environments

On 10 July 2006, the boundary-layer development in Niamey was typical of what we observe in those regions, when the soil is still dry and surface heating is significant. As an illustration, Fig. 3 shows the observations of the UHF wind profiler in high mode during the entire day, which gives a picture of the diurnal cycle of the low-to-middle troposphere. We observe the typical nocturnal low-level jet up to about 700 m until 1000 UTC (Kassimou et al. 2010), which brings

water vapor at low levels by advection during the night. This advected water vapor is a major source of humidity (Parker et al. 2005), as the ground is still very dry at that time (not shown). During the day, dry convection mixes the water vapor and distributes it vertically. This was consistently observed with the UHF wind profilers and radiosoundings during the AMMA Enhanced Observing Period, as described by Lothon et al. (2008). A nocturnal jet with a maximum wind speed around 400 m above the ground was found in the early morning at 0600 UTC on average. During the day, the turbulent mixing by dry convection is responsible for a decrease of the wind within the PBL, as seen from 0800 UTC to 1200 UTC in Fig. 3. Figure 3 also shows the diurnal decrease of the African Easterly Jet (AEJ) at 4 km height after 1500 UTC, put into evidence by Kalapureddy et al. (2009), and likely due to momentum transfers between the boundary layer and the free troposphere. The open circles in Fig. 3 show that the PBL depth reached more than 2500 m, before the deep convective system around 1600 UTC disturbs the interpretation of the reflectivity profiles, as revealed by the large scatter of the open circles then. It also modifies the wind profiles, as seen in the same figure, with a decrease of the east component and increase of the north component from 4 to 5 km, and the wind turning easterly and northerly in respectively the upper and lower part of the boundary layer. The deep growth of the PBL and high cloud base (not shown) reached that day are consistent with the analysis of Guichard et al. (2009).

The radiosoundings shown in Fig. 4 complement the wind profiler observations, and quantify the warming and drying of the PBL on this day: an increase

of 4 K on potential temperature and a decrease of 2 g kg^{-1} in water vapor mixing ratio r_v are observed in the mixed layer between 1130 and 1730 UTC (Fig. 4a). The wind shear at the top of the mixed layer is large (Fig. 4b), favoring the momentum exchange through entrainment, as do the vertically developing clouds. At 1730 UTC, the footprints of the deep convective system can be seen through the very stable layer near surface at 1730 (Fig. 4a), with a potential temperature at least 8 K smaller than into the mixed layer, linked with the moister and cooler DC. The close-to-neutral SAL overlying the mixed layer from 2.5 km up to 4.2 km (Fig. 4a), favors the rapid growth of the clouds from their base to the SAL inversion at 4.2 km. The amount of energy needed to overcome this inversion can come from their initial triggering energy and/or from their turbulent and mesoscale environment. In the other hand, during the monsoon onset, the dry SAL is also expected to favor evaporation and downdraft formation, as discussed by Marsham et al. (2008).

The convective available potential energy (CAPE) and convective inhibition (CIN) calculated from the radiosoundings revealed a decrease for both between 0600 UTC and 1800 UTC (not shown), from 1700 to 1000 J kg^{-1} for the former, and from 70 to a minimum of 12 J kg^{-1} for the latter.

The observation of meteorological variables near the surface during the entire day made by the ARM Facility are shown in Fig. 5. Until the passing of the deep convective system S_0 marked by sharp changes at about 16h30 UTC, the near-surface air warms and dries as explained above, with an increase of $10 \text{ }^\circ\text{C}$ at surface from sunrise to 16h30 UTC, and a minimum of humidity close to 20

% in mid-afternoon (Fig. 5b). The nocturnal jet does not reach the ground, as generally observed by Lothon et al. (2008), but rather leads to a small peak in wind speed at the start of the day around 0900 UTC. Later, the mean wind is a little weaker, but thermal gusts make larger fluctuations, typical of daytime turbulence (Fig. 5a). The signature of the deep convective system is manifested by a northerly gust reaching around 8 m s^{-1} , and a sharp decrease in temperature and increase in relative humidity. The equivalent potential temperature found at surface after S_0 is consistent with air coming from above the PBL (not shown). After S_0 , two smaller deep convective C_1 and C_2 cells crossed the radar area (see later in section 4, and Fig. 11), with effects detected at respectively 1710 and 1810 UTC at the ground (see Fig. 5), and associated gust front detected at respectively 1730 and 1830 UTC. Finally, in the evening after the passage of the strong cold pool outflow, unperturbed conditions prevail at the surface.

As shown, the meteorological conditions on this day contrast with tropical convection in moist environment, with in particular a deep boundary layer with cloud base reaching around 2.5 km and a decreasing Convective Available Potential Energy through the day. Other features (not shown), such as a weak latent heat flux (maximum no larger than 30 W m^{-2} , according to eddy correlation flux measurement system at the ARM site), large sensible heat flux (reaching 350 W m^{-2}) and an increasing level of free convection, also reveal conditions specific to semi-arid environments. Note that there is no African Easterly Wave propagating over the region that day.

These conditions contrast with a number of studies emphasizing a daytime

increase of CAPE over land in the Tropics or in the midlatitudes in Summer (Machado et al., 2002; Guichard et al., 2004). In addition, the large convective inhibition prevailing around midday do not seem favorable to deep convection triggering.

c. Morning dry convection and early afternoon shallow convection

For several days in July 2006, the MIT radar observations showed coherent band-like eddies (streaks or rolls) forming within the convective boundary layer every morning and evolving to more isotropically-distributed cells in late morning and early afternoon. This was the case of 10 July. Figure 6 displays the radar reflectivity perturbation field at 600 m a. g. l at 1040 UTC, 1220 UTC, 1430 UTC and 1540 UTC on 10 July in a $100 \text{ km} \times 100 \text{ km}$ domain, with a grid resolution of 200 m obtained after removing a 50-point average (10 km). This allowed us to partly remove the effect of a large scale artificial spatial variability of the reflectivity field, which was symmetric to the mean wind axis, and likely due to the asymmetric shape of the backscattering insects or other objects.

Contrary to rolls, cells should not show any axisymetry. In between both, band-like structures show axisymetry, but do not extend longitudinally as much as ‘true’ rolls (they have a much smaller aspect ratio than rolls have). This is how we distinguish between the types of structures.

Clear air rolls can be identified with an orientation aligned mainly with the mean wind. (The mean wind can be retrieved from the volume velocity processing

(VVP, Waldteufel and Corbin, 1979) or from the UHF profiler measurements.) Indeed, rolls were observed from 0900 UTC to about 1330 UTC (Fig. 6a and b), while deepening and parting with increasing PBL depth. Starting at 1100, the evidence of rolls is less clear, but band-like organized structures can be seen in certain sectors (Fig. 6b). The rolls then change into cells in the early afternoon (Fig. 6c and d), with increasing instability. The criterion given by Weckwerth (1999) that rolls change to cells when $Z_i/L \leq 25$ (where L is the Monin-Obukov scale, and Z_i is determined from the wind profiler data) corresponds to a transition time of 1030 UTC in our case, which approximately corresponds to the time when cells start to dominate, even if rolls (or bands) are still present at some places. At all times, the organization is heterogeneous, with varying type of organization and varying scale around the radar. Figure 6 shows the evolution from rolls to cells and from smaller to larger horizontal scales of those structures. It also reveals several distinct regions where, for a given time, the size of the structures or their separation distance are larger than the scales of surrounding structures. This is the case, for example, in the East area, relative to the North area in general, and especially in the North-East sector at 15h40 UTC, where structures have larger scales. Later in the day, deep convection was actually triggered over those regions where boundary-layer structures displayed the larger scales (circled in Fig. 6c and d), which suggests that convective initiation is sensitive to subtle fluctuations in PBL characteristics at the meso- and submeso- scale. In other words, clear air larger scale structures may be part of the building of deep convective cells later in the afternoon.

2D auto-correlation function of the reflectivity field at 600 m a.g.l. enabled us to attempt to quantify the characteristic scales associated with the structures—that is, the predominant wavelength for streaks and the most probable distance between the cells later in the day (see Atkinson and Zhang, 1996). For streaks, we define two dimensions: one longitudinally to the streaks, and one transverse to them. This defines two separation distances for the band-like structures: the transverse separation distance (or roll wavelength for rolls), and the longitudinal separation distance, that is the distance from one band to the other along their longitudinal axis. Results are shown in Fig. 7, in which the scales between the rolls or the cells and the angle relative to north are plotted as a function of time, over the duration of the growth of the convective boundary layer. Scales are normalized by Z_i . Two sectors, SE and NW, were chosen and considered separately, showing the heterogeneity of the spatial organization. (The SW sector had missing data (Fig. 6), and the NE sector was where the deep convection started.) In each sector, a 40 km by 40 km area was considered for the calculation of the 2D autocorrelation function. Due to second-trip echoes in the NW region, we did not analyze the 2D autocorrelation function in this sector after 1330 UTC. We find consistent and uniform roll-type organization from 0900 UTC to 1100 UTC with a separating distance increasing from 1.8 to 2.2 km and Z_i increasing from 800 m to 1300 m, maintaining the normalized scales constant $\simeq 2$ (Fig. 7a). Later, the scales are larger and much more scattered. The first clouds were observed around 1130 UTC by the ARM 95 GHz radar (not shown), and may contribute significantly to this change. Until 1330 UTC, a certain band-

like organization is still discernible in the reflectivity and 2D autocorrelation fields, with larger separation distances increasing up to around 6-8 km— that is, about 3 to 4 Z_i . After that time, cells predominate, with scales leveling around 6-8 km and sometimes forming a line with the same direction as that of the preceding clear air band-like organization (Fig. 7b). The leveling of the scales concomitant with increasing Z_i makes the normalized scales decrease during this phase (Fig. 7a). This can correspond to clouds starting to develop more vertically than horizontally.

In the afternoon, a few cells grew vertically significantly in the clear air exploration zone of the MIT, but dissipated within 10-30 minutes. The first high reflectivity patch which grew toward the storm system S_0 , further described in the following section, was found centered at about 5 km height (see Fig. 8 at 1540 UTC). It was linked to surface, but with some spatial discontinuity at the inversion, possibly due to shear (inducing tilt) and different echo sources across the overpassed inversion (inducing a change in radar reflectivity). The Doppler velocity (not shown) locally increases in the low-level reflectivity structure that seems to be linked with the deep cell. This apparent lack of continuity in the reflectivity signal from the PBL to the core of the upper level maximum suggests that gravity waves above the PBL could be involved in the initiation process of the system. However, we found no sign of such mesoscale forcing. Rather, we found more evidence that this system was actually triggered by local processes and likely by a surface temperature anomaly.

Figure 9 shows the land surface temperature and soil moisture retrieved from

satellite imagery at 1200 UTC, with superimposed trajectory of the S_0 system. It reveals a warm anomaly of about 5 °C at the starting position of the deep convective cell. This suggests a significant role played by surface heating heterogeneity, along with favorable PBL processes. According to the 1130 UTC radiosounding, a surface temperature excess of 2°C could overwhelm the *CIN*. Later, the increasing temperature was probably partly compensated by the concomitant drying of the low troposphere, but likely, the extra-heating in some areas was able to trigger updrafts capable of breaking the inversion.

Contrasts of surface temperature favor convective activity, but moisture can also play a significant role. The soil moisture field in Fig. 9 mainly results from preceding rains, which occurred in particular in the night between 8 and 9 July (not shown). This leads to a link between land surface temperature and soil moisture (Taylor et al. 2003) (surfaces that got rain have larger soil moisture and negative temperature anomaly), although other processes come into play (like vegetation cover, topography, ...). We partly observe this anti-correlation in Fig. 9: the warm region is also dryer, which generates larger sensible heat flux than over surrounding moister and cooler surfaces. This lends further support to the significant role of surface heating heterogeneity in triggering S_0 .

Soil moisture variability, beyond its impact on surface temperature heterogeneity, can add a supplemental contribution to the convective initiation, as previously found by e. g. Weckwerth (2000), and by Taylor and Ellis (2006) in Sahel especially (see also Taylor et al., 2010). The MIT radar is located close to a large gradient of soil moisture, on the dry side. This gradient makes a NS

moisture-boundary to the west of the triggering region and a EW boundary to the south. In this configuration, the west-southwesterly monsoon wind, coming from wetter surfaces, brings moister air over the dryer and warmer surface, favoring deep convection.

At large scale, the moisture boundary is orientated EW (NS gradient). The system travelled roughly along this large-scale gradient, and north of it. Note, though, that its direction and velocity are mainly controlled by the mid-troposphere AEJ flow. The vertical velocity measured by the UHF wind profiler reveals large and persistent updrafts with values between 1 and 2 m s⁻¹ for about 1 hour-duration in the early afternoon (Fig. 10a), which contrast with the typical weak velocity measured in the mixed layer at this wavelength, usually negatively biased by a few tens of cm s⁻¹ (see observations by e. g. Lothon et al., 2001; and an explanation by Cheinet and Cumin, 2010). For comparison, Fig. 10b shows an example of a typical clear day, with no deep convection (13 July 2006). This lends support to the existence of strong updrafts occurring prior to the start of S_0 (1540 UTC), at the time of the preceding first quickly growing cells (1330 to 1500 UTC). The large downdraft later in the afternoon is also significantly stronger (down to below -3 m s⁻¹, with no contribution of precipitation according to the radar reflectivity) than that which would be observed on a clear day, and is likely associated with the subsidence on the side of deep convective systems, including S_0 .

4. Afternoon deep convection

a. Evolution of the deep convection triggering and propagation

Figure 11 shows the reflectivity pattern in horizontal cross-sections at 600 m height and vertical zonal cross-sections 5 km to the north of the radar, at selected times in the late afternoon (1600, 1640, 1700, 1720, 1740, 1820 UTC).

Due to the consistent presence of insects and other passive material targets in the lower troposphere, the MIT radar data allow us to study the fine-scale structure of the clear air up to 3 km vertically and 50 km horizontally describing the entire boundary layer (Geerts and Miao 2005). In the free troposphere above the PBL, the echo is too weak for the radar to detect, except within the deep convective cells where both clear air echo sources and hydrometeors are concentrated. The radar is then able to track the velocity of precipitation structures which usually move westward with the AEJ.

The first deep cell developed at 1540 UTC 2 km west of the MIT radar ($X=-2$ km $Y=0$ km in Fig. 6d), reaching 5 km altitude and possibly stopped by the SAL inversion. It propagated westward and dissipated by 1600 (Fig. 11a). The main system S_0 considered in this study was detected at low levels (within the PBL) at 1550 UTC 18 km east with a double cell (not shown). Three low level semi-circular bands formed at its (east) backside, about 10 km apart (Fig. 11a, b, c), likely due to the generation of a wave at the rear of the system. This cell S_0 grew up to 30 km long along the north-south direction, and 10 to 20 along the east-west axis (Fig. 11h). This size is rather small relative to the mesoscale

convective systems that can form in this region, and to still larger squall lines (see the SEVIRI MSG images in Fig. 12). But those small systems are much more numerous and can still contribute significantly to the transport of dust and water vapor.

A marked circular and divergent gust front accompanied this cell, as clearly observed after 1700 UTC (Fig. 11c, g, h, i). The vertical cross-sections suggest that the gust front depth was 1.5 km in the corresponding E-W axis. A second deep convective cell (noted C_1) then began exactly at the east flank of that circular outflow and also at the same location as S_0 (Fig. 11c,f), moving north of the radar at 1710 UTC. (Clouds predating C_1 can be seen in Fig. 11e at $X=18$ km and $Z=5$ km.) At 1730 UTC, a third similar cell (noted C_2) also started in that flank (Fig. 11h, with predating clouds in Fig. 11f and j at respectively $X=30$ km and $X=23$ km, $Z=5$ km), moving north of the radar at 1840 UTC while the intensity of the first main cell was starting to decrease. This sequence of radar observations suggests that those two secondary cells C_1 and C_2 were generated by the first pocket of cold air associated with the density current of S_0 . More precisely, they seem to result from the interaction of the outflow of S_0 with the three low-level circular wave bands mentioned previously (Fig. 11c), even if this remains hypothetical, with some similarity with previous studies such as Taylor et al. (2010) or Marsham and Parker (2006). The wind profile is very similar to Marsham and Parker (2006), and leads to stronger low-level wave effects in their case with initiation on the eastward side of the existing system, consistent with our observations. Also note that S_0 , C_1 and C_2 all started at the same

location, which is consistent with a significance of surface features. Systems C_1 and C_2 did not exceed 10 km in width and quickly dissipated. Finally, a fourth cell C_3 (not shown, but with predated clouds in Fig. 11l) started in the rear of C_2 , about 4 km north from the MIT, and moved westward. Cells C_1 , C_2 and C_3 were decaying rapidly after 1740 UTC (Figs. 11h, k), 1850 UTC (not shown) and 1930 UTC (not shown), respectively. The observation of these short-lived cells was conditioned by the nearly absent low-level wind shear. In some respects, this is consistent with the theory of Rotunno et al. (1988) that long-lived and deeper convective cells occur where cell's cold surface outflow interacts with the low-level shear. In the absence of such shear, the spreading of cold outflow's circulation inhibits deep vertical penetration of the environmental air into the cell.

The passage of S_0 , C_1 and C_2 through Niamey meteorological station at 1640, 1710 and 1810 UTC can be seen in Fig. 5, as well as a wind gust at 1730 UTC, with a 0.6 °C cooling, a 8 m s⁻¹ gust and a 0.3 hPa pressure rise, typical of gust fronts (Wakimoto 1982). This pressure anomaly P_{ano} was calculated by removing a 30-min sliding mean from the atmospheric pressure. Following a decrease in intensity and velocity, the eastern portion of the gust front reappeared clearly on the MIT radar data and was still in the scope of the radar at 2100 UTC 55 km away to the south-east (not shown).

The gust front likely continued to move south-eastward for a short period, but could not be observed after 2110 UTC as it was probably below the lowest elevation angle scan of the radar (A 1500 m height gust front can be seen out to 120 km range with the lowest beam, but only out to 55 km if it is 500 m high).

The gust front was not recorded by aerosol instruments settled in Banizoumbou (13.52 °N, 2.63 °E, see Figs. 2, 9 and 11i), 50 km to the east to the east (86°) of the radar, nor on the meteorological variables. According to the MIT radar PPIs, Banizoumbou was located very close to the northern limit of this gust front southeastern segment, and may have been only a few km away from it. This portion of the gust front was not visible on SEVIRI images. The pressure rise of 0.3 hPa showed on the surface station indicates that the energy of this gust front was not very strong at 1730 UTC. Together with the previous satellite and radar observations, this supports the hypothesis that it dissipated shortly after 2100 UTC, about 60 or 70 km away from the radar. As said before, the surface equivalent potential temperature observed at 1730 UTC corresponds to air coming from above the PBL inversion or higher (not shown), but the circular shape of the gust front indicates that the mixing by the convective cells was not efficient enough to transfer enough momentum from the AEJ down to the low-troposphere to increase the extension of the gust front along the E-W axis. The expansion coefficient along this axis is only slightly larger than along the North-South axis. Still, the observations made by the UHF profiler show how the low-troposphere wind turned to North or Easterly in the afternoon, from the time of occurrence of S_0 around 1600 UTC until around 2000 UTC (Fig. 3).

On its western flank, the main system S_0 generated another gust front at 17h20 (Fig. 11g), a few km to the west of the cell. It moved quickly out of the scope of the radar. But according to SEVIRI images, it seems to have triggered another deep cell S_1 at 19h30 UTC (see Fig. 12b) which actually inhibited the

former and propagated northwestward, with a gust front in its northwestern flank that was still visible at 2345 UTC on SEVIRI MSG images (Fig. 12d).

b. Analysis of the Doppler velocity with MUSCAT

An indication of the airflow associated with the convective system can be first sketched out from RHI measurements performed during the 10-min radar observation cycles. Figure 13 displays an example of an RHI section of reflectivity (top) and Doppler velocity (bottom) made at 300° azimuth and 1710 UTC. According to Fig. 11c, this vertical section sliced the northern edge of the convective cell to the west of the radar. A typical feature is the evident diverging outflows near the surface and at the cell top (10 km altitude) associated respectively with convective downdraft and updraft air detrainment, as revealed by the positive/negative Doppler velocity feature.

As discussed in Section 2, application of MUSCAT to derive the 3D wind structure from volume scans requires the evaluation of the advection speed of the storm system so as to obtain pseudo multiple-Doppler observations in a reference frame moving with the system. However, Fig. 11 clearly shows that the most active cell S_0 to the west of the radar between 1700 and 1740 UTC moved westward while the apparent gust front materialized as quasi-circular rings tended to expand radially. Examination of the low-level reflectivity from the scans starting at 1710, 1720, and 1730 UTC reveals that the western edge moved mainly westward at 7.6 m s^{-1} and slightly to the south at 1.6 m s^{-1} , while the expansion

factor (relating the size of the gust front at two successive scans) was about 1.2 in the west-east direction and 1.1 in the south-north direction in 10 min. (Both advection and homothetic transformation are taken into account with respect to the reference time of 1720 UTC, by reducing or expanding the grid resolution respectively at 1710 and 1730 UTC, by use of the above factors.)

The retrieved absolute and relative wind structures are shown superimposed on the reflectivity field in an horizontal cross-section at 200 m height and a vertical cross-section at $Y=5$ km in Fig. 14. The method was validated a posteriori by re-calculating the Doppler velocity obtained at each time from the retrieved field.

The retrieved internal circulation is also well defined inside the circular gust front where most of the flow perturbations occurs, and strongly differs from the less-perturbed environmental flow. The airflow in the west-east cross-section appears quite consistent with the RHI representation in Fig. 13. The expected outflow is well described within the circular pattern. It is more intense on its western flank, probably due to the subsidence associated with the most active part of the cell which was about 10 km by 30 km wide at 1720 UTC and more than 10 km deep. This favored its westward propagation. According to Fig. 14a, the wind is generally weak around the system and its cold pool. Figure 14d clearly shows the strong upward motion in the front of the main convective cell, accelerating with height. It reveals a complex circulation inside the cold pool, and around new triggered cells. Outside the cold pool, Fig. 14b shows some flow splitting upwind in the western edge and a convergence line along the front. The

relative winds in the vertical cross section (Fig. 14d) indicate that the downdraft air from the main cell tended to spread out near the surface, while the updraft aloft is nearly upright, consistently with the absence of low-level wind shear (e. g. Rotunno et al., 1988). Smaller vertical motions are associated with the secondary C_1 cell.

c. Further analysis of the density current

This case provides an opportunity to compare the characteristics of the observed DC with a simple model recently proposed by Grandpeix and Lafore (2010) for the parameterization of the DCs. Our objective here is to verify, based on this simple model, that the characteristics of the observed circular outflow (manifestation at surface, vertical profile, horizontal extension,...) are consistent together and with the potential of this DC to trigger new convection.

Density currents are often called ‘wakes’ in the context of parameterizing the effect of deep convection— that is, in a broader point of view, the ‘wake’ of convective system. In Grandpeix and Lafore (2010)’s model, wakes are defined by their density within the grid cell, their fractional area σ_w , their depth h_w , the change of temperature and water vapor mixing ratio within the wake relative to their environment, their expansion rate C_* and their propagation speed V_w . C_* is thus the mean spreading speed of the wake leading edge (gust front here), while V_w is the translation speed of the whole cold pool.

The wake potential energy (WAPE) is defined as the mean potential energy

deficit in the DC region:

$$WAPE = -g \int_0^{h_w} \frac{\delta\theta_v(z)}{\bar{\theta}_v} dz, \quad (1)$$

where θ_v is the virtual potential temperature, $\bar{\theta}_v$ is the mean virtual potential temperature and $\delta\theta_v$ is the difference between the virtual potential temperature in the cold pool and the virtual potential temperature of the environment:

$$\delta\theta_v(z) = \theta_{vw}(z) - \bar{\theta}_v. \quad (2)$$

$\bar{\theta}_v$ is assumed constant in the boundary layer due to mixing. h_w is the mean wake depth, defined by $\delta\theta_v(z = h_w) = 0$.

Following von Kármán (1940), the wake spreading speed is proportional to the square root of the *WAPE*:

$$C_* = k_* \sqrt{2WAPE}, \quad (3)$$

where k_* is a coefficient.

In our case, we evaluate the expansion rate of a single almost circular DC, from the change of area covered by the wake with time. The previous analysis with MUSCAT revealed a slightly larger expansion coefficient along the east-west direction than along the north-south direction. However, in order to test this model, we can assume the wake area to be circular, as supported by the horizontal cross sections shown in Fig. 11. We processed the images in a way similar to that shown in this figure, coloring the pixels that are within the circular gust front black and the pixels that are off the wake white. This enabled us to estimate the area covered by the wake and the cell, relative to the $100 \text{ km} \times 100$

km window considered around the radar. However, the estimated area covers both the convective cell and the wake, rather than the wake alone. Due to the presence of a gust front all around the cell and to the circular shape of the entire area, we find it more convenient to consider this area rather than the area occupied by the wake alone. This method still enables us to evaluate the expansion rate of the wake, since the gust front surrounds the cell here.

At 1700 UTC, this area was 1100 km², and increased to 2200 km² at 1720 UTC and to 3200 km² at 1740 UTC. Assuming a circular wake, this leads to radii of respectively 18 km, 26 km and 32 km. We deduced an expansion rate varying from 6.7 m s⁻¹ around 1710 UTC to 4.4 m s⁻¹ around 1730 UTC, which gives $C_* \simeq 5.6$ m s⁻¹ between 1700 and 1740 UTC. The western edge of the system was not entirely seen by the radar after this time, which limits our estimates to this period. Those estimates of C_* are consistent with a bulk estimate that can be obtained from a simple governing equation given by Goff (1976) for the gust front propagation speed as a function of the maximum speed observed normal to the front:

$$C_* = 0.67 U, \quad (4)$$

with $U = 8$ to 10 m s⁻¹ deduced from the MIT radar radial velocity within the DC (and consistent with the 8 m s⁻¹ gust and 0.3hPa pressure rise observed at the surface—as given by Bernouilli equation), we find C_* between 5.4 and 6.7 m s⁻¹.

The radiosounding made at 1730 UTC by ARM Facility can be considered as

the vertical profile observed behind the system. Note that this is the exact time of the observation of the gust at the surface (Fig. 5). It allows us to estimate the WAPE at that time from equation 1, and to compare it to the theory given by equation 3. h_w can be estimated either from the MIT reflectivity within the edge of the wake or by the vertical profile of θ_v . Figure 15a shows the vertical cross section of the reflectivity at $X = -7$ km and at 1720 UTC, with the same interpolation parameters as for Fig. 11, and Fig. 15b shows the vertical profile of θ_v measured with the 1730 UTC radiosounding. From the θ_v profile, we can estimate h_w to 1.5 km, which is consistent with the higher reflectivity found in the wake edge up to about 1.5 km as well, as seen at $Y = -18$ km and $Y = 34$ km in this cross section (see also the horizontal cross section in Fig. 11g and h for reference). This local maximum of reflectivity is due to the concentration of insects, and other biological or terrestrial fragments in the convergence line of the gust front. After integrating the profile of θ_v up to $h_w=1.5$ km and with $\bar{\theta}_v=313$ K, we found $WAPE=36.6$ J kg⁻¹ with equation 1. With C_* previously estimated to 4.4 m s⁻¹ at 1730 UTC, this gives $k_*=0.52$ with equation 3. This is consistent with previous estimates found in the literature: Lafore and Moncrieff (1989) found $k_*=0.68$ and $k_*=0.33$ was also found recently (unpublished computation by J. P. Lafore, personal communication).

Looking more closely into the structure of the circular gust front with the MIT radar reflectivity, we observed a large variability in space and time of the height h_w . Some of this variability can be seen in Fig. 11g, h, and i, since the reflectivity intensity is a good index of the depth reached by the wake. A

decrease of reflectivity in time over these three panels is observed, as well as variation along the circle. At 1720 UTC, h_w could reach 2 to 2.5 km in the southwest and northwest, but was only a few hundred meters in the northeast and southeast and even non-existent in some places. Such a decrease of the gust intensity in its eastern part is further evidence that the gust front did not travel very far, and indeed not as far as the aerosol surface station of Banizoumbou.

Finally, the analysis of Fig. 11h in the previous section shows that the low-level gust fronts can themselves trigger new cells. Indeed, this is consistent with our calculation of the *WAPE* at 1730 UTC. As argued by Grandpeix and Lafore (2010), if the available lifting energy, taken equal to the *WAPE*, is larger than the *CIN*, then the energy associated with the wake is able to trigger deep convection. According to Guichard et al. (2009), the *CIN* is around 50 J kg^{-1} at 1200 but decreases to about 12 J kg^{-1} at 1730 UTC, which makes it possible for the DC to trigger deep convective cells, as observed with the MIT radar, for example in Fig. 11c and h.

5. Concluding remarks

This study presents the first documentation and discussion of a unique case study, in which a convective system is observed during most of its life-cycle in range of MIT radar, at high resolution in time and space in an intensively instrumented site. At first glance, the case seemed like a textbook event, but it turned out to show a large variability in space and a complex circulation within

the cold pool, with several systems triggered in its wake.

The data suggest a key role played by surface temperature and moisture heterogeneity and boundary-layer dynamics on deep convection triggering, consistently with previous studies in Sahel. Organized boundary-layer rolls in the morning later turned to cells with larger characteristic sizes in certain areas. The deep PBL growth (up to 2500 m depth) and persistent strong updrafts in the afternoon were also characteristic of this day. We observed a clear 5 °C surface temperature anomaly at the start of the trajectory of the system S_0 , that offers further evidence of the role of surface heating and heterogeneity in the deep convection triggering during the pre-onset period, where the influence of AEWs and air moisture are not as large as during the active phase of the monsoon, when larger systems like MCSs or squall lines frequently occur. This temperature anomaly is linked with a dry soil pattern, and a warm/cold wet/dry boundary that also may play a significant role in the triggering. In addition, the gust outflow appears to play an important role in the triggering of new convective cells.

Using a simple wake parameterization, we were able to evaluate the WAPE associated with the DC generated by S_0 and showed that it was capable of triggering new deep convective cells on its flank, as indeed observed by the MIT radar. Consistent with the size (10 km \times 30 km) and energy of the system, the DC characteristics, such as propagation speed (about 5 to 7 m s⁻¹), pressure rise (0.3 hPa) and wind gust (about 10 m s⁻¹), were not very large compared to those associated with MCSs or squall lines. Because the 10th of July started very typ-

ically of the semi-arid region during the pre-onset period, our analysis suggests that the smaller systems like S_0 are very common in this region and during this period; though rather small, they are numerous and participate significantly in the transfers of momentum, temperature, humidity and aerosol, and in generating a large number of gust fronts that can themselves trigger new convective cells as we clearly observed here. Our next analyses will consider the entire pre-onset period to confirm this hypothesis, and evaluate their contribution, as well as revise the deep convection initiation processes in those conditions.

It is important to better understand how such deep convective systems trigger in order to improve the parameterization of the transition from shallow to deep convection. A study based on joint observations, 1D column numerical simulation and Large Eddy Simulation (LES) is ongoing to better understand and parameterize the initiation of deep convection, in this case of large forcing by surface-atmosphere interaction and weak advection (see Guichard et al., 2009). Even if our analysis revealed the complexity and spatial variability of the event, this case can serve as a valuable, well documented testbed for parameterizations of wakes. We consider this a golden opportunity for studying the initiation of deep convection and wakes, and for testing and improving their respective parameterizations.

Acknowledgments.

Laboratoire d'Aérologie is funded by INSU-CNRS and University of Toulouse. Based on a French initiative, AMMA was built by an international scientific group and is currently funded by a large number of agencies, especially from France, UK, USA and Africa. It has been the beneficiary of a major financial contribution from the European Community's Sixth Framework Research Programme. Detailed information on scientific coordination and funding is available on the AMMA International web site <http://www.amma-international.org>. The authors also thank the Massachusetts Institute of Technology and NASA Hydrology for supporting the operation of the radar in Niamey. We thank Brian Russell for his organization and archival of the MIT radar data. We thank the Atmospheric Radiation Measurement Facility for operating the UHF wind profiler, radiosoundings and surface stations, and for supplying the data. We also thank Jean-Louis Rajot for his feedbacks on aerosol measurements made at Banizoumbou experimental site, Louis Gonzalez and Christine Deroo for the SEVIRI imagery. Finally, we thank Tammy Weckwerth and an anonymous reviewer for their numerous and relevant comments and suggestions.

REFERENCES

- Alonge, C. J., K. I. Mohr, and W. K. Tao, 2007: Numerical studies of wet versus dry soil regimes in the West African Sahel. *J. Hydrol.*, **8**, 102-116.
- Aminou, D. M. A., 2002: MSG's SEVIRI instrument. *ESA Bull. - European Space Agency*, **111**, 15-17.
- Angevine, W. M., A. B. White, and S. K. Avery, 1994: Boundary-layer depth and entrainment zone characterization with a boundary-layer profiler. *Boundary-Layer Meteor.*, **68**, 375-385.
- Atkinson, B. W. and J. W. Zhang, 1996: Mesoscale shallow convection in the atmosphere. *Rev. Geophys.*, **34**, 403-431.
- Balsley, B. B. and K. S. Gage, 1982: On the use of radars for operational wind profiling. *Bull. Amer. Meteor. Soc.*, **63**, 1009-1018.
- Bousquet, O. and M. Chong, 1998: A multiple-Doppler synthesis and continuity adjustment technique (MUSCAT) to recover wind components from Doppler radar measurements. *J. Atmos. Oceanic Technol.*, **15**, 343-359.
- Cheinet, S. and P. Cumin, 2010: Local structure parameters of temperature and humidity in the entraining boundary layer: LES analysis. *Submitted to J. App. Meteor. Clim.*

- Chen, T. C., S. Y. Wang, and A. J. Clark, 2000: North Atlantic hurricanes contributed by African easterly waves north and south of the African easterly jet. *J. Climate*, **21**, 6767-6776.
- Chong, M., 2010: The 11 August 2006 squall-line system as observed from MIT Doppler radar during the AMMA SOP. *Quart. J. Roy. Meteor. Soc.*, **136**, 190-208.
- Chong, M. and O. Bousquet, 2001: On the application of MUSCAT to a ground-based dual-Doppler radar system. *Meteorol. Atmos. Phys.*, **78**, 133-139.
- Comer, R. E., A. Slingo, and R. P. Allan, 2007: Observations of the diurnal cycle of outgoing longwave radiation from the Geostationary Earth Radiation Budget instrument. *Geophys. Res. Letter*, **34**, L02 823.
- Cook, K., 1999: Generation of the African Easterly Jet and its role in determining West African precipitation. *J. Clim.*, **12**, 1165-1184.
- Cooper, H. J., M. Garstang, and J. Simpson, 1982: The diurnal interaction between convection and peninsular-scale forcing over South Florida. *Mon. Wea. Rev.*, **110**, 486-503.
- Cressman, G. P., 1959: An operational objective analysis system. *Mon. Wea. Rev.*, **87**, 367-374.
- Doviak, R. J. and D. S. Zrnić, 1993: *Doppler radar and weather observations*. Academic Press, 398-404 pp.

- Elía, R. and I. Zawadzki, 1997: Some theoretical aspects of wind retrieval from single Doppler radar data. *Proceedings of the 28th Int. Conf. on Radar Meteor., Amer. Meteor. Soc., Boston, MA USA*, 416–417.
- Fink, A. H. and A. Reiner, 2003: Spatio-temporal variability of the relation between African easterly waves and west African squall lines in 1998 and 1999. *J. Geophys. Res.*, **108**.
- Geerts, B. and Q. Miao, 2005: Airborne radar observations of the flight behavior of small insects in the atmospheric convective boundary layer. *Env. Ent.*, **34**, 361–377.
- Goff, R. C., 1976: Vertical structure of thunderstorm outflows. *Mon. Wea. Rev.*, **104**, 1429–1440.
- Gossard, E. E., R. B. Chadwick, W. D. Neff, and K. P. Moran, 1982: The use of ground-based doppler radars to measure gradients, fluxes and structure parameters in elevated layers. *J. Appl. Meteor.*, **21**, 211-226.
- Grandpeix, J. Y. and J.-P. Lafore, 2010: A density current parameterization coupled with Emanuel’s convection scheme. Part I: The models. *J. Atmos. Sci.*, DOI: 10.1175/2009JAS3044.1.
- Guichard, F., F. Couvreux, C. Rio, D. Bouniol, A. Gounou, B. Campistron, M. Chong, and M. Lothon, 2009: The 10 July 2006 case study: data analysis and modelling set up. *AMMA Project no. 004089. Deliverable D.2.1.A.k.*

- Guichard, F., et al., 2004: Modelling the diurnal cycle of deep precipitating convection over land with CRMs and SCMs. *Quart. J. Roy. Meteorol. Soc.*, **130**, 3139–3172.
- Imaoka, K., A. Shibata, N. Nakagawa, Y. Nakajima, H. Haijima, H. Tanaka, and T. Imatani, 2000: Airborne microwave radiometer for AMSR and AMSR-E project. *Proceedings of the Society of Photo-optical Instrumentation Engineers (SPIE)*, **4152**, 303–309.
- Jacoby-Koaly, S., B. Campistron, S. Bernard, B. Bénech, F. Girard-Ardhuin, and J. Dessens, 2002: Turbulent dissipation rate in the boundary layer via UHF wind profiler Doppler spectral width measurements. *Boundary-Layer Meteorol.*, **103**, 361–389.
- Janicot, S. and B. Sultan, 2007: The large-scale context of the West African Monsoon in 2006. *Exchanges CLIVAR newsletter*, **12 (2)**, 11–17.
- Kalapureddy, M. C., M. Lothon, B. Campistron, F. Lohou, and F. Said, 2009: Wind profiler observations of the African Easterly Jet and its interactions with the boundary-layer and Saharan heat low. *Quart. J. Roy. Meteorol. Soc.*, DOI [10.1002/qj.486](https://doi.org/10.1002/qj.486).
- Kalthoff, N., et al., 2009: The impact of convergence zones on the initiation of deep convection: A case study from COPS. *Atmos. Res.*, **93**, 680–694.
- Kassimou, A., D. J. Parker, B. Brooks, N. Kalthoff, and T. Lebel, 2010: The

- diurnal cycle of lower boundary-layer wind in the West African monsoon. *Quart. J. Roy. Meteor. Soc.*, **136**, 66–76.
- Lafore, J.-P. and M. W. Moncrieff, 1989: A numerical investigation of the organization and interaction of the convective and stratiform regions of tropical squall lines. *J. Atmos. Sci.*, **46**, 521–544.
- Lavaysse, C., A. Diedhiou, T. Laurent, and T. Lebel, 2006: African Easterly Waves and convective activity in wet and dry sequences of the West African Monsoon. *Climate Dynamics*, **27**, 319–332.
- Lima, M. A. and J. W. Wilson, 2007: Convective storm initiation in a moist tropical environment. *Mon. Wea. Rev.*, **136**, 1847–1864.
- Lothon, M., B. Campistron, S. Jacoby-Koaly, B. Bénéch, F. Lohou, and F. Girard-Ardhuin, 2001: Comparison of radar reflectivity and vertical velocity with a scannable C-band Doppler radar and two UHF profilers in the lower troposphere. *J. Atmos. Oceanic Technol.*, **19**, 899–910.
- Lothon, M., F. Said, F. Lohou, and B. Campistron, 2008: Observation of the diurnal cycle in the low troposphere of West Africa. *Mon. Wea. Rev.*, **136**, 3477–3500.
- Machado, L. A. T., H. Laurent, and A. A. Lima, 2002: Diurnal march of the convection observed during TRMM-WETAMC/LBA. *J. Geophys. Res.*, **107** (doi:10.1029/2001JD000338).

- Marshall, J. H. and D. J. Parker, 2006: Secondary initiation of multiple bands of cumulonimbus over southern Britain. part II : Dynamics of secondary initiation. *Quart. J. Roy. Meteor. Soc.*, **132**, 1053–1072.
- Marshall, J. H., D. J. Parker, C. M. Grams, C. M. Taylor, and J. M. Haywood, 2008: Uplift of Saharan dust south of the inter-tropical discontinuity. *J. Geophys. Res.*, **113** (doi:10.1029/2008JD009844).
- Mathon, V., A. Diedhiou, and H. Laurent, 2002: Relationship between easterly waves and mesoscale convective systems over the Sahel. *Geophys. Res. Lett.*, **29**, doi:10.1029/2001GL014371.
- Moncrieff, M. W. and C. Liu, 1999: Convection initiation by density currents: role of convergence, shear, and dynamical organization. *Mon. Wea. Rev.*, **127**, 2455–2464.
- Parker, D. J., et al., 2005: The diurnal cycle of the West African Monsoon circulation. *Quart. J. Roy. Meteorol. Soc.*, **131**, 2839–2860.
- Pellarin, T., T. Tran, J. M. Cohard, S. Galle, J. P. Laurent, P. de Rosnay, and T. Vischel, 2009: Soil moisture mapping over West africa with a 30-minute temporal resolution using AMSR-E observations and a satellite-based rainfall product. *Hydrol. Earth Syst. Sci.*, **13**, 1887–1896.
- Reed, R. J., D. C. Norquist, and E. E. Recker, 1977: The structure and properties of African wave disturbances as observed during phase III of GATE. *Mon. Wea. Rev.*, **105**, 317333.

- Rotunno, R., J. B. Klemp, and M. L. Weisman, 1988: A theory for strong, long-lived squall lines. *J. Atmos. Sci.*, **45**, 463–485.
- Sultan, B., S. Janicot, and P. Drobinski, 2007: Characterization of the diurnal cycle of the West African Monsoon around the monsoon onset. *J. Climate*, **20**, 4014–4032.
- Taylor, C. M. and R. J. Ellis, 2006: Satellite detection of soil moisture impacts on convection at the mesoscale. *Geophys. Res. Letter*, **33**, L03 404.
- Taylor, C. M., R. J. Ellis, D. J. Parker, R. R. Burton, and C. D. Thorncroft, 2003: Linking boundary-layer variability with convection: A case-study from JET2000. *Q. J. R. Meteorol. Soc.*, **129**, 2233–2253.
- Taylor, C. M., P. P. Harris, and D. J. Parker, 2010: Impact of soil moisture on the development of a Sahelian mesoscale convective system: A case-study from the AMMA Special Observing Periods. *Q. J. R. Meteorol. Soc.*, **136**, 56–470.
- Taylor, C. M., D. J. Parker, and P. P. Harris, 2007: An observational case study of mesoscale atmospheric circulations induced by soil moisture. *Geophys. Res. Letter*, **35**, L15 801.
- Thorncroft, C. D., 1995: An idealized study of African easterly waves. III: More realistic basic states. *Q. J. R. Meteorol. Soc.*, **121**, 1589–1614.
- Trigo, I. F., C. C. Peres, L. F. an DaCamara, and S. C. Freitas, 2008: Thermal land surface emissivity retrieved from sevir/meteosat. *IEEE Trans. Geosci. Remote Sens.*, **46**, DOI: 10.1109/TGRS.2007.905 197.

- von Kármán, T., 1940: The engineer grapples with non-linear problems. *Bull. Amer. Math. Soc.*, **46**, 615–683.
- Wakimoto, R., 1982: The life-cycle of thunderstorm gust fronts as viewed with Doppler radar and rawinsonde data. *Mon. Wea. Rev.*, **110**, 1060–1082.
- Waldteufel, P. and H. Corbin, 1979: On the analysis of single-Doppler radar data. *J. Appl. Meteor.*, **18**, 532–542.
- Weckwerth, T. M., 1999: An observational study of the evolution of horizontal convective rolls. *Mon. Wea. Rev.*, **127**, 2160–2179.
- Weckwerth, T. M., 2000: The effect of small-scale moisture variability on thunderstorm initiation. *Mon. Wea. Rev.*, **128**, 4017–4030.
- Weckwerth, T. M., H. V. Murphey, C. Flamant, J. Goldstein, and C. R. Pettet, 2008: An observational study of convection initiation on the 12 June 2002 during IHOP_2002. *Mon. Wea. Rev.*, **136**, 2283–2304.
- Weckwerth, T. M. and D. B. Parsons, 2006: A review of convection initiation and motivation for IHOP_2002. *Mon. Wea. Rev.*, **134**, 5–22.
- Weckwerth, T. M., et al., 2004: An overview of the international h2o project (IHOP_2002) and some preliminary highlights. *Bull. Amer. Meteor. Soc.*, **85**, 253–277.
- Wilson, J. W., B. G. Foote, N. A. Crook, J. C. Fankhauser, C. G. Wade, J. D. Tuttle, and C. K. Mueller, 1992: The role of boundary-layer convergence zones

and horizontal rolls in the initiation of thunderstorms: a case study. *Mon. Wea. Rev.*, **120**, 1785–1815.

Wilson, J. W. and R. D. Roberts, 2006: Summary of convective storm initiation and evolution during IHOP: Observational and modeling perspective. *Mon. Wea. Rev.*, **134**, 23–47.

List of Figures

1	<i>Temperature at 950 hPa (gray scale) and mean sea level pressure (contours) over West Africa on 10 July 2006 (from ECMWF analysis). The white thick lines indicates the position of the ITD (line of constant dew point temperature at 2 m, equal to 15°C). The dashed black frame indicates the contour of the satellite images shown in Fig. 12.</i>	48
2	<i>(a) Map of Niger (source: http://en.wikipedia.org/wiki/Niger). The MIT radar, the wind profiler, the radiosounding station and the meteorological stations were all co-located at Niamey airport. (b) Topography around Niamey. ‘+’ locates the MIT radar and ‘▲’ locates the ARM site.</i>	49
3	<i>Time-height cross section of the horizontal wind observed by the ARM UHF wind profiler in Niamey on 10 July 2006. Arrows represent the mean wind (leftward arrow for easterly winds, and upward arrow for southerly wind), and colorscale indicates the wind speed. The open circles indicate the PBL top estimated from the structure coefficient of the air refractive index, estimated from the radar reflectivity. The solid black line indicated the time of the passage of the system S_0 at surface, and the dashed lines indicate C_1 and C_2 (see Fig. 5).</i>	50

- 4 *Radiosoundings at Niamey at (solid lines) 1130 UTC and (dashed lines) 1730 UTC: (a) (black lines) Temperature and water vapor (gray line), (b) (black) zonal and (gray) meridian wind components. The wind profiles are also directly represented in (b) with straight gray lines at each height (left profile is at 1130 UTC, right profile is at 1730 UTC).* 51
- 5 *Time series of (a) (black line) wind speed and (gray line) direction, (b) (black line) temperature and (gray line) relative humidity, on 10 July 2006 at Niamey airport. In (b), the pressure anomaly is added on a supplemental small sub-diagram from 1500 to 2100 UTC (black thin line). Vertical dashed lines indicate the passage of systems S_0 , C_1 and C_2 , discussed later (see also Fig. 11). The vertical solid line indicates the signature of a gust associated with the density current, and is also the exact time of the 1730 UTC radiosounding launch. This time is indicated with an arrow at the top (labelled ‘RS’).* 52
- 6 *Horizontal cross section at 600 m a. g. l. of sub-mesoscale fluctuations in reflectivity, at (a) 1040, (b) 1220, (c) 1340 and (d) 1540, obtained with $R_{xy} = 600$ m and $R_z = 350$ m. High reflectivity in the NW sector at 1340 and 1540 UTC are second-trip echoes from long-distance deep convective systems. Circled area are regions of interest discussed in the text. The dashed line in (d) represents the cross-section in Fig. 8.* . . . 53

7	<p><i>Evolution of (a) the normalized scales of the structure spacing deduced from 2D autocorrelation of the reflectivity at 600 m and (b) the angle of the bands or of the alignment of cells relative to the north. In the framed legend of (a), ‘transverse’ indicates the transverse separating distance between bands, ‘longitudinal’ indicates the longitudinal separating distance from one to the next band, or from cell to cell. When there is no obvious roll-type organization, the distance between cells is estimated from the distance between the first and secondary maximum of the 2D autocorrelation function (often found aligned with the mean wind). Scales are normalized by Z_i. The solid line in (a) indicates the initiation of S_0 cell.</i></p>	54
8	<p><i>E-W vertical cross section $Y=5$ km away from the MIT radar at 1540 UTC. $R_{xy}= 1000$ m and $R_z= 1000$ m are used here.</i></p>	55
9	<p><i>(a) Land surface temperature (colorscale) deduced from MSG and soil moisture (isolines, volumic percentage) at 1200 UTC. Bright isolines stand for dry soil, darker for moister soil. White squares are missing data due to clouds. The diamonds show the trajectory of S_0 deep convective system, the triangle indicates the MIT radar location, and the closed circle indicates Banizoumbou.</i></p>	56
10	<p><i>Vertical velocity observed by the UHF wind profiler at low mode, on (a) 10 July and (b) 13 July 2006. In (a), the solid black line indicates the time of the passage of the system S_0, and the dashed lines indicate C_1 and C_2 (see Fig. 5).</i></p>	57

11	<p><i>Reflectivity interpolated in (first and third rows) horizontal cross section at $Z=500$ m a. g. l. and (second and fourth rows) vertical cross section at $Y=5$ km, at (a, d) 1600, (b, e) 1640, (c, f) 1700, (g, j) 1720, (h, k) 1740 and (i, l) 1820 UTC. The MIT radar is positioned at the reference point ($X=0$, $Y=0$). $R_{xy}=600$ m and $R_z=350$ m are used here for the horizontal section, $R_{xy}=1000$ m and $R_z=1000$ m for the vertical section. Dashed lines indicate vertical and horizontal cross-sections shown. The diagonal dashed line in panel (c) indicates the RHI of Fig. 13.</i></p>	58
12	<p><i>Seviri MSG images over West Africa at (a) 1730 UTC, (b) 1930 UTC, (c) 2100 UTC and (d) 2315 UTC (see Fig. 1 to locate the considered area). The arrows point to either S_0 or S_1. In (d), GF indicates the thin arc manifesting S_1 gust front. Channels used for are a combination of visible ($0.65 \mu\text{m}$, $0.81 \mu\text{m}$, $1.63 \mu\text{m}$) and infrared ($10.8 \mu\text{m}$), but the figure is shown in black and white.</i></p>	59
13	<p><i>(a) Reflectivity and (b) Doppler velocity in the RHI section at 1710 UTC and 300° azimuth (see dashed line in Fig. 11c). Positive Doppler velocity indicates receding flow. Note the presence of aliased at low elevation angles.</i></p>	60
14	<p><i>Horizontal (top) and vertical (bottom) cross section of the absolute wind (left) and system-relative wind (right) obtained with MUSCAT analysis, superimposed on reflectivity and representative of the half hour centered at 1720 UTC. Horizontal dashed line in the top panels indicate the position of the vertical cross section shown in bottom panels.</i></p>	61

15 (a) *Vertical cross section of the reflectivity at $X = -7$ km at 1720 UTC. (b) Vertical profile of the virtual potential temperature at 1730 UTC. The WAPE is represented by the shaded surface. The edge of the wake is visible in (a) with the local maximum of reflectivity at $Y = -18$ and $Y = 34$ km, extending from the ground to about 1.5 km a.g.l.* . . . 62

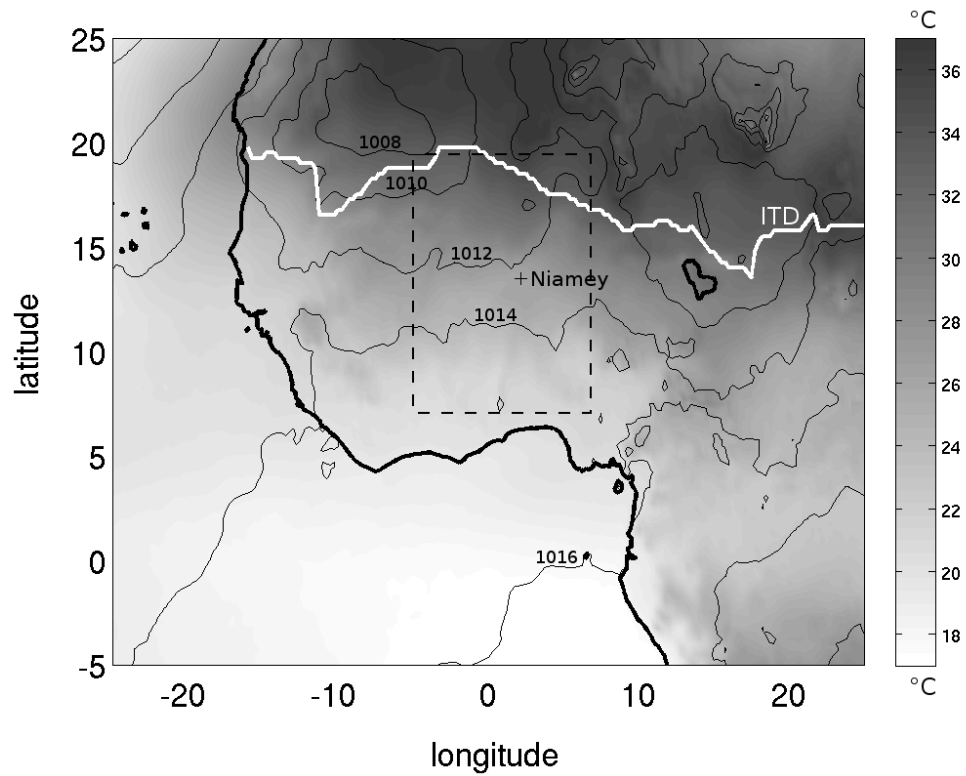


FIG. 1. *Temperature at 950 hPa (gray scale) and mean sea level pressure (contours) over West Africa on 10 July 2006 (from ECMWF analysis). The white thick lines indicates the position of the ITD (line of constant dew point temperature at 2 m, equal to 15°C). The dashed black frame indicates the contour of the satellite images shown in Fig. 12.*

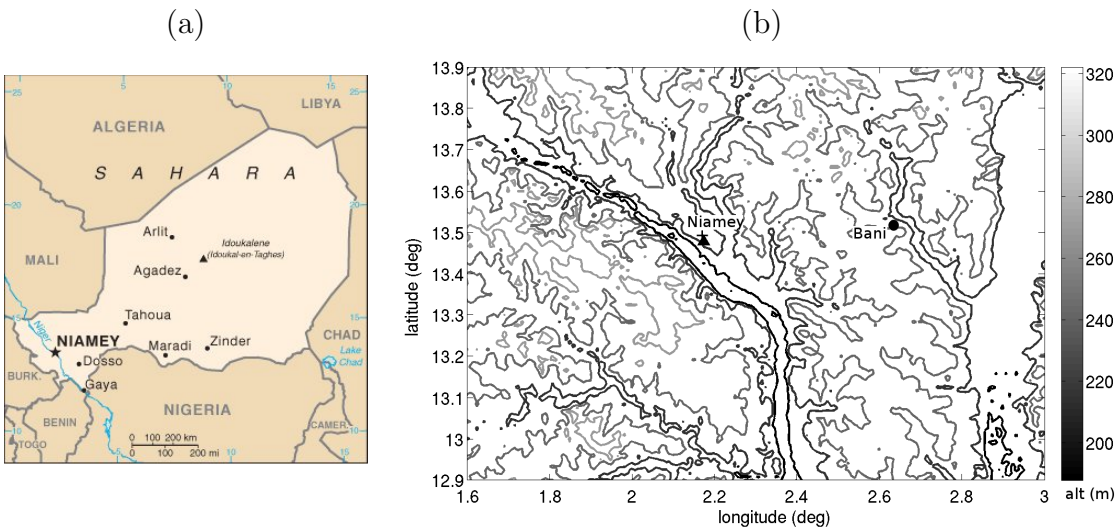


FIG. 2. (a) Map of Niger (source: <http://en.wikipedia.org/wiki/Niger>). The MIT radar, the wind profiler, the radiosounding station and the meteorological stations were all co-located at Niamey airport. (b) Topography around Niamey. '+' locates the MIT radar and '▲' locates the ARM site.

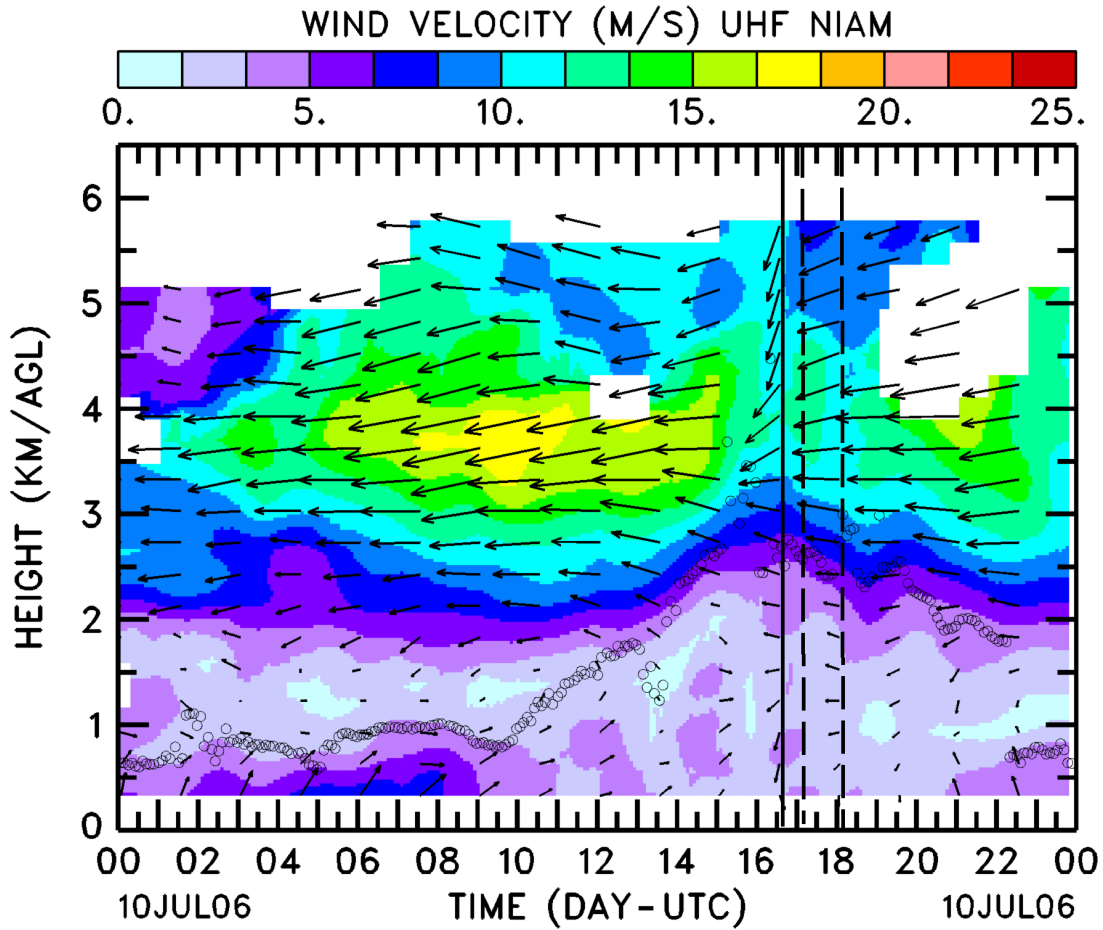


FIG. 3. *Time-height cross section of the horizontal wind observed by the ARM UHF wind profiler in Niamey on 10 July 2006. Arrows represent the mean wind (leftward arrow for easterly winds, and upward arrow for southerly wind), and colorscale indicates the wind speed. The open circles indicate the PBL top estimated from the structure coefficient of the air refractive index, estimated from the radar reflectivity. The solid black line indicated the time of the passage of the system S_0 at surface, and the dashed lines indicate C_1 and C_2 (see Fig. 5).*

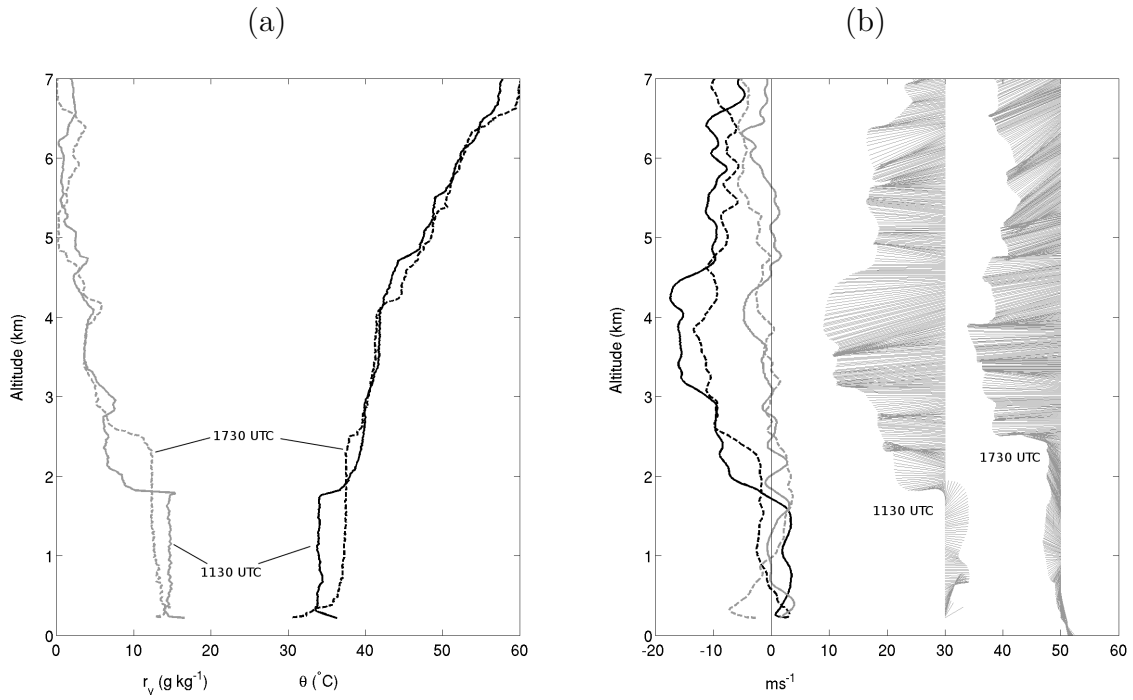


FIG. 4. Radiosoundings at Niamey at (solid lines) 1130 UTC and (dashed lines) 1730 UTC: (a) (black lines) Temperature and water vapor (gray line), (b) (black) zonal and (gray) meridional wind components. The wind profiles are also directly represented in (b) with straight gray lines at each height (left profile is at 1130 UTC, right profile is at 1730 UTC).

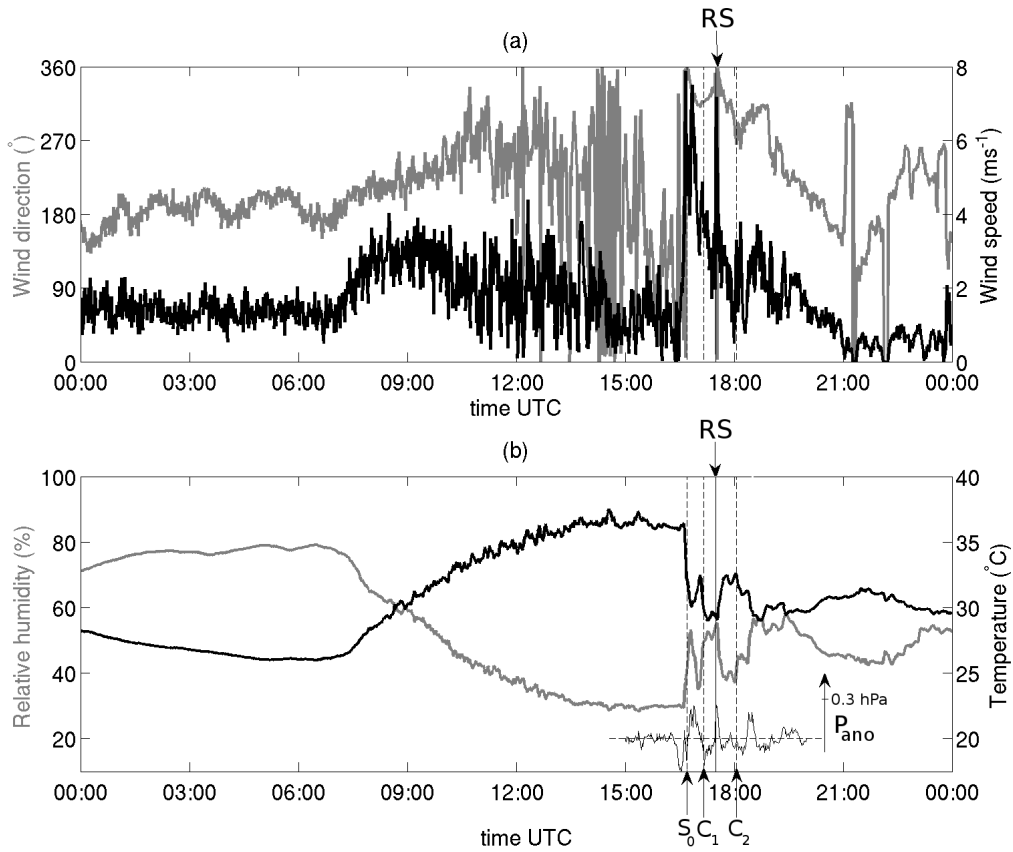


FIG. 5. Time series of (a) (black line) wind speed and (gray line) direction, (b) (black line) temperature and (gray line) relative humidity, on 10 July 2006 at Niamey airport. In (b), the pressure anomaly is added on a supplemental small sub-diagram from 1500 to 2100 UTC (black thin line). Vertical dashed lines indicate the passage of systems S_0 , C_1 and C_2 , discussed later (see also Fig. 11). The vertical solid line indicates the signature of a gust associated with the density current, and is also the exact time of the 1730 UTC radiosounding launch. This time is indicated with an arrow at the top (labelled ‘RS’).

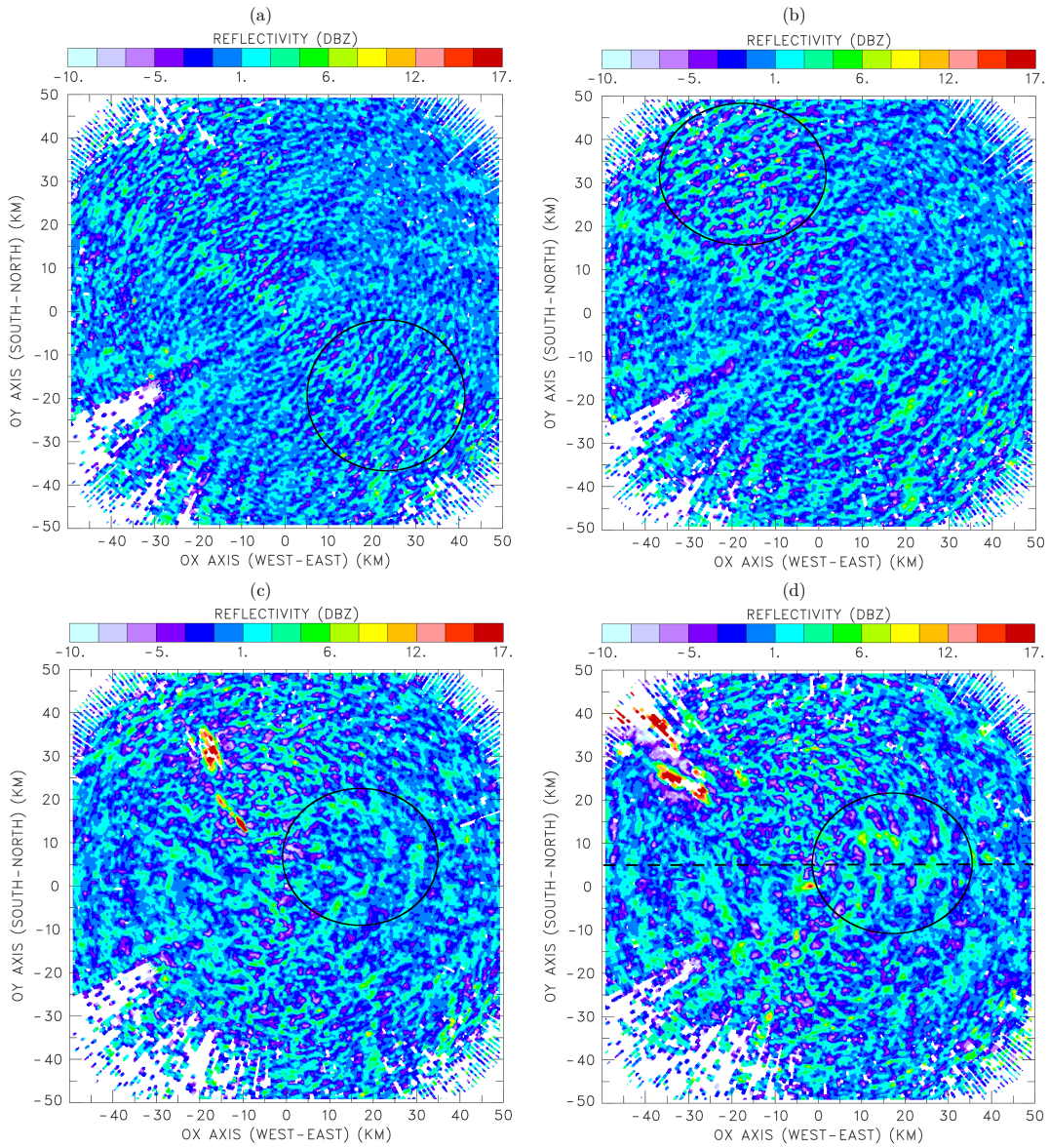


FIG. 6. *Horizontal cross section at 600 m a. g. l. of sub-mesoscale fluctuations in reflectivity, at (a) 1040, (b) 1220, (c) 1340 and (d) 1540, obtained with $R_{xy} = 600$ m and $R_z = 350$ m. High reflectivity in the NW sector at 1340 and 1540 UTC are second-trip echoes from long-distance deep convective systems. Circled area are regions of interest discussed in the text. The dashed line in (d) represents the cross-section in Fig. 8.*

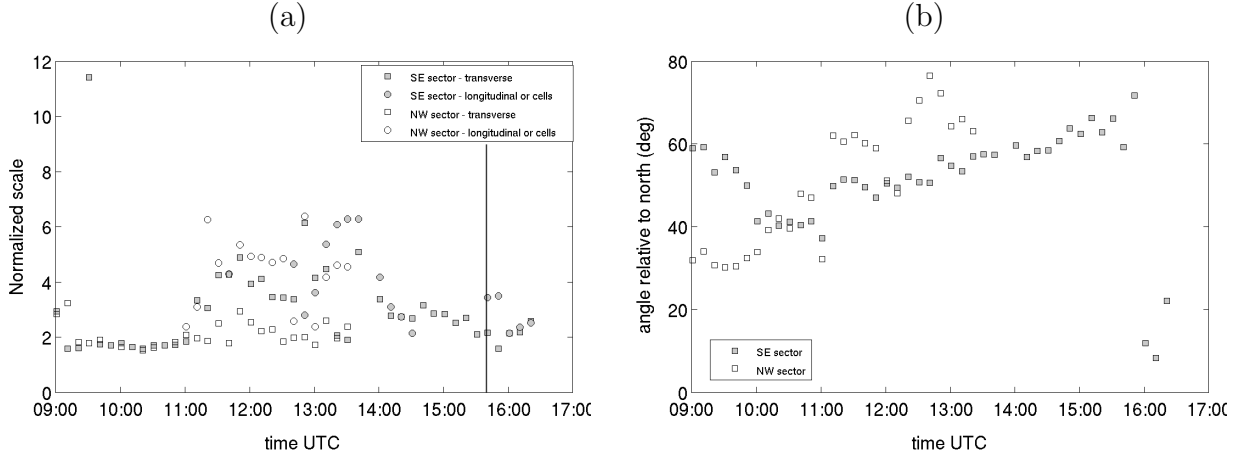


FIG. 7. Evolution of (a) the normalized scales of the structure spacing deduced from 2D autocorrelation of the reflectivity at 600 m and (b) the angle of the bands or of the alignment of cells relative to the north. In the framed legend of (a), ‘transverse’ indicates the transverse separating distance between bands, ‘longitudinal’ indicates the longitudinal separating distance from one to the next band, or from cell to cell. When there is no obvious roll-type organization, the distance between cells is estimated from the distance between the first and secondary maximum of the 2D autocorrelation function (often found aligned with the mean wind). Scales are normalized by Z_i . The solid line in (a) indicates the initiation of S_0 cell.

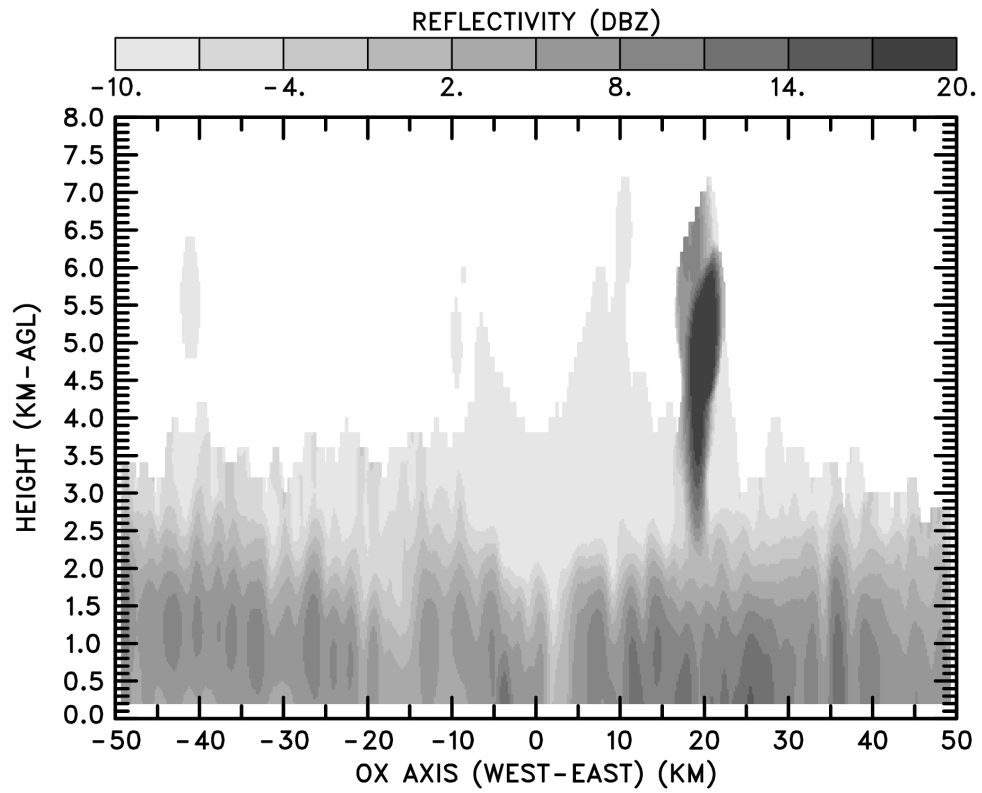


FIG. 8. *E-W vertical cross section $Y=5$ km away from the MIT radar at 1540 UTC. $R_{xy}=1000$ m and $R_z=1000$ m are used here.*

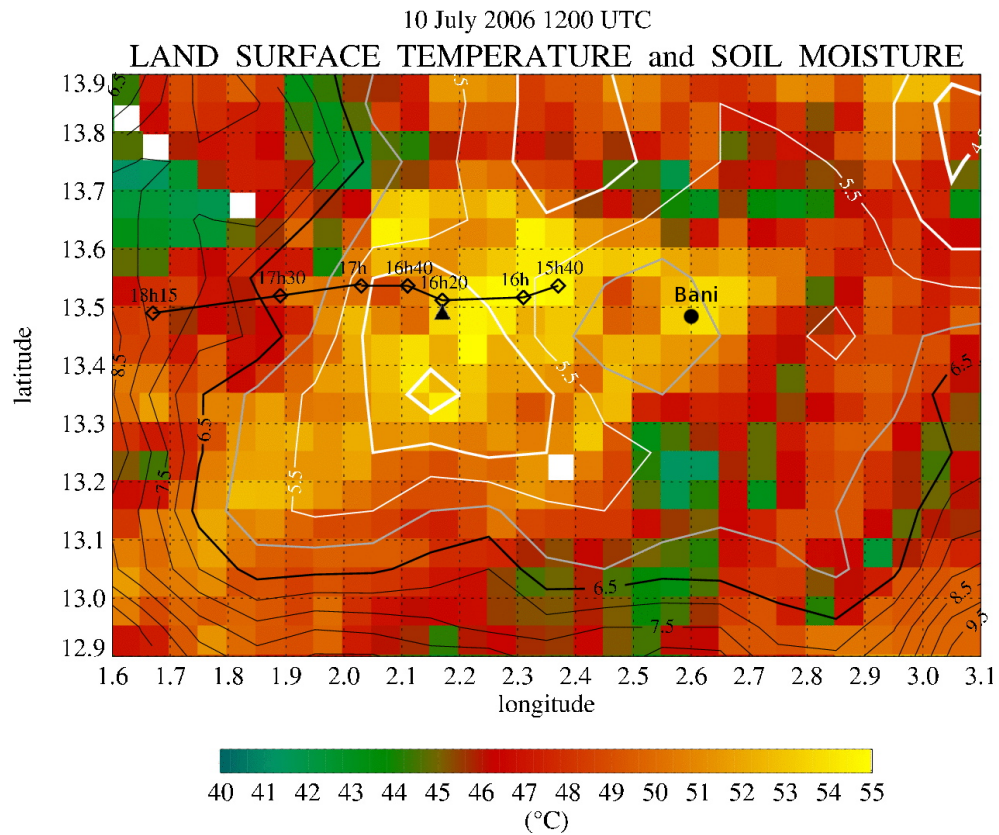


FIG. 9. (a) Land surface temperature (colorscale) deduced from MSG and soil moisture (isolines, volumic percentage) at 1200 UTC. Bright isolines stand for dry soil, darker for moister soil. White squares are missing data due to clouds. The diamonds show the trajectory of S_0 deep convective system, the triangle indicates the MIT radar location, and the closed circle indicates Banizoumbou.

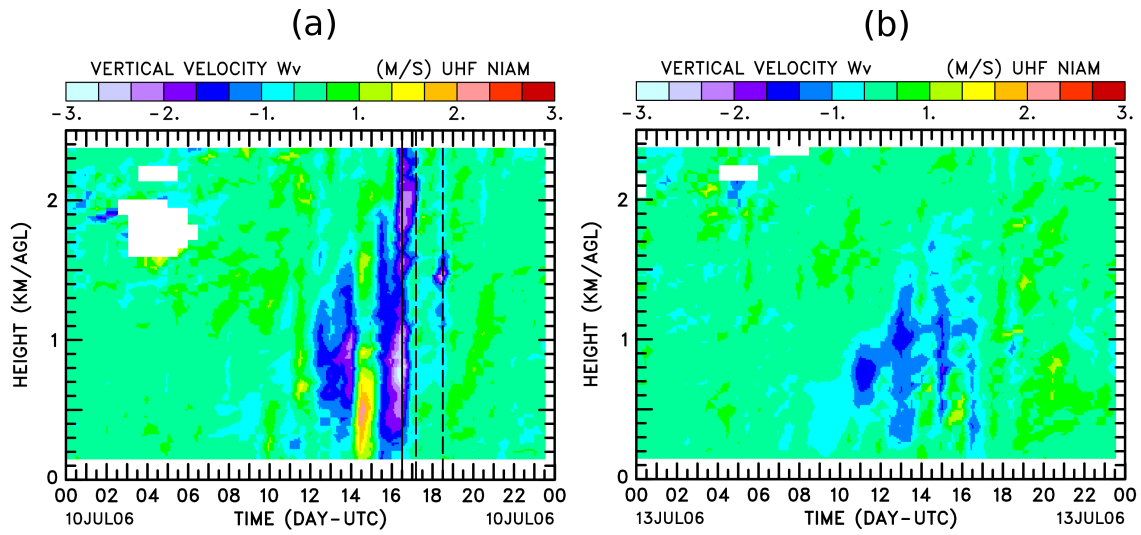


FIG. 10. Vertical velocity observed by the UHF wind profiler at low mode, on (a) 10 July and (b) 13 July 2006. In (a), the solid black line indicates the time of the passage of the system S_0 , and the dashed lines indicate C_1 and C_2 (see Fig. 5).

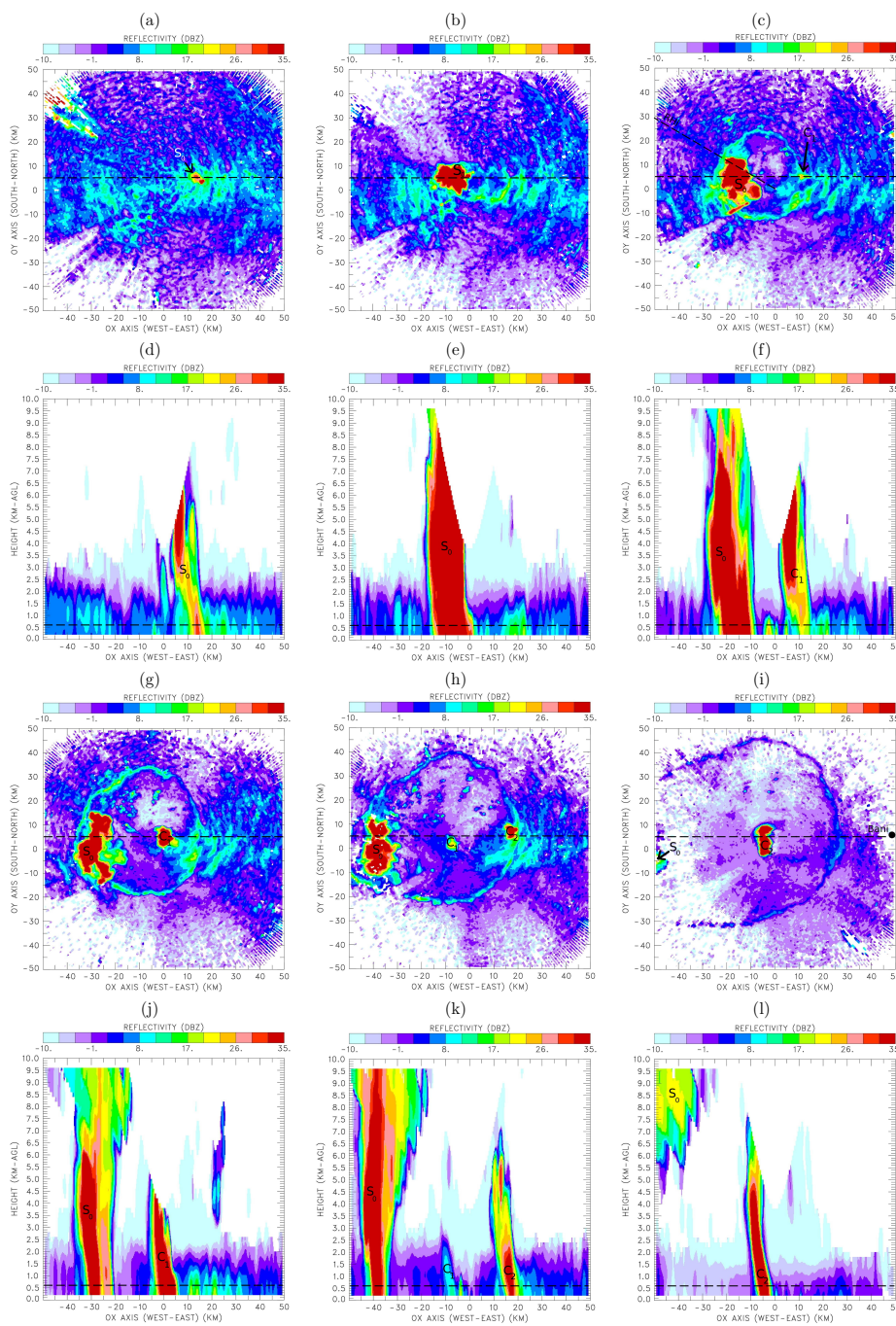


FIG. 11. Reflectivity interpolated in (first and third rows) horizontal cross section at $Z=500$ m a. g. l. and (second and fourth rows) vertical cross section at $Y=5$ km, at (a, d) 1600, (b, e) 1640, (c, f) 1700, (g, j) 1720, (h, k) 1740 and (i, l) 1820 UTC. The MIT radar is positioned at the reference point ($X=0$, $Y=0$). $R_{xy}=600$ m and $R_z=350$ m are used here for the horizontal section, $R_{xy}=1000$ m and $R_z=1000$ m for the vertical section. Dashed lines indicate vertical and horizontal cross-sections shown. The diagonal dashed line in panel (c) indicates the RHI of Fig. 13.

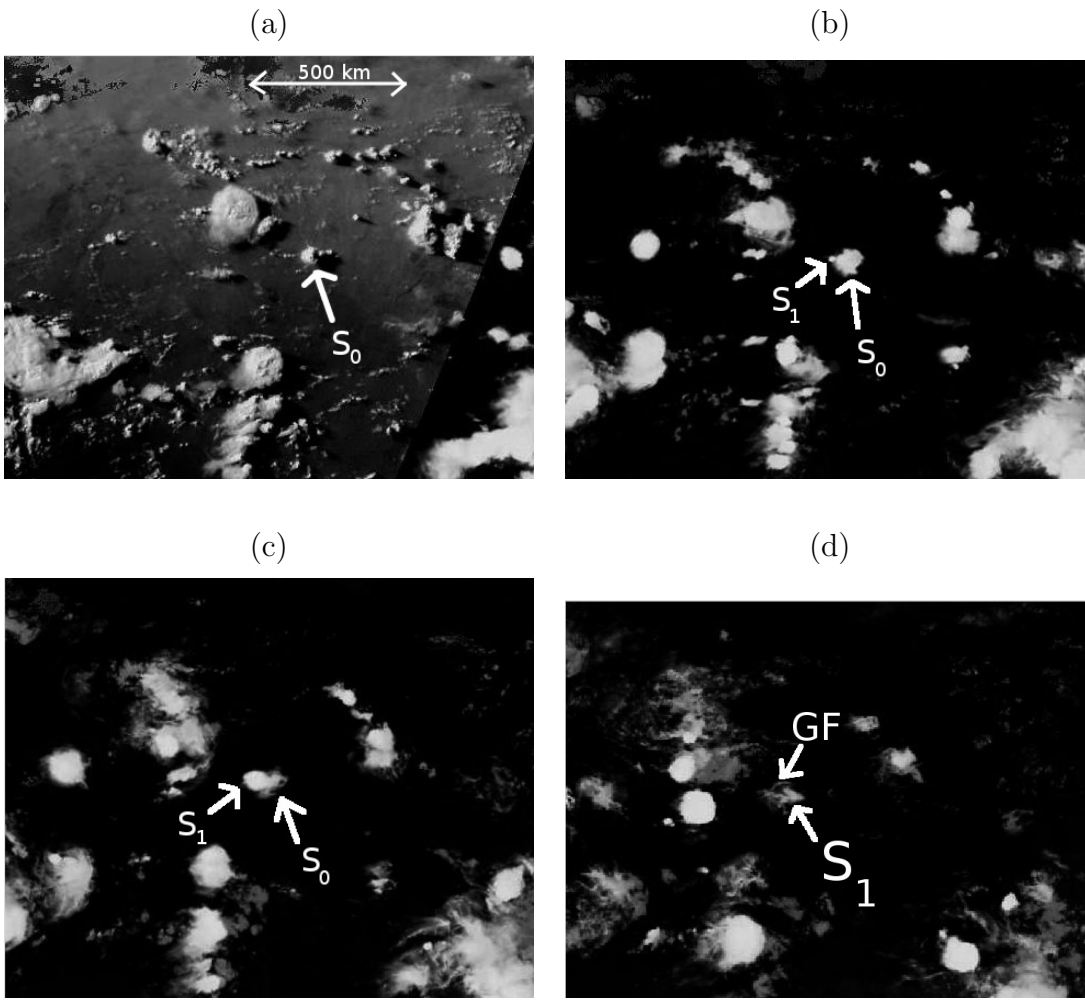


FIG. 12. *Seviri MSG images over West Africa at (a) 1730 UTC, (b) 1930 UTC, (c) 2100 UTC and (d) 2315 UTC (see Fig. 1 to locate the considered area). The arrows point to either S_0 or S_1 . In (d), GF indicates the thin arc manifesting S_1 gust front. Channels used here are a combination of visible ($0.65 \mu\text{m}$, $0.81 \mu\text{m}$, $1.63 \mu\text{m}$) and infrared ($10.8 \mu\text{m}$),—turned to gray scale representation here.*

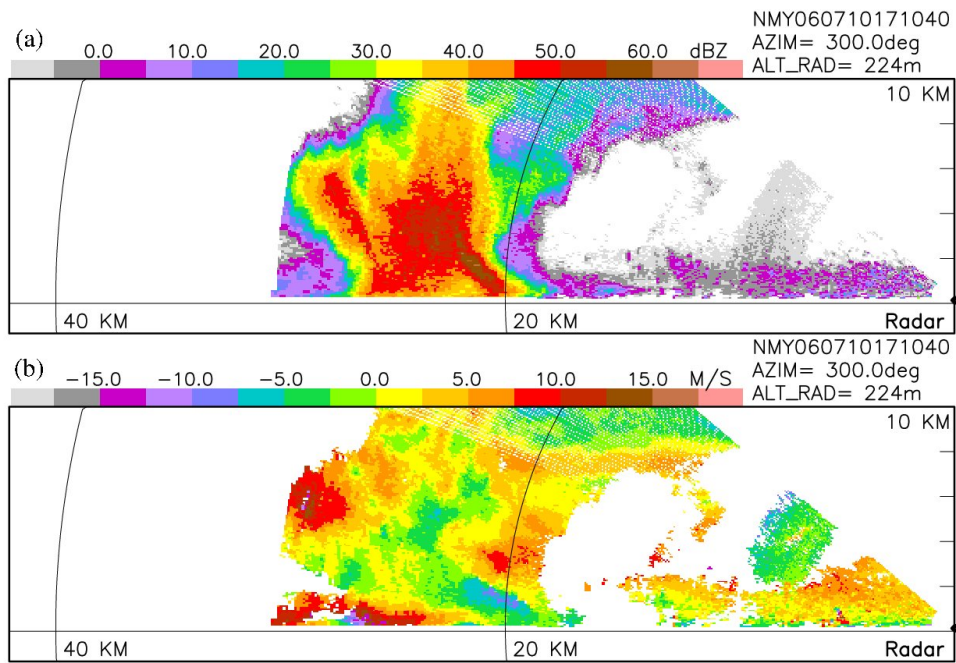


FIG. 13. (a) Reflectivity and (b) Doppler velocity in the RHI section at 1710 UTC and 300° azimuth (see dashed line in Fig. 11c). Positive Doppler velocity indicates receding flow. Note the presence of aliased at low elevation angles.

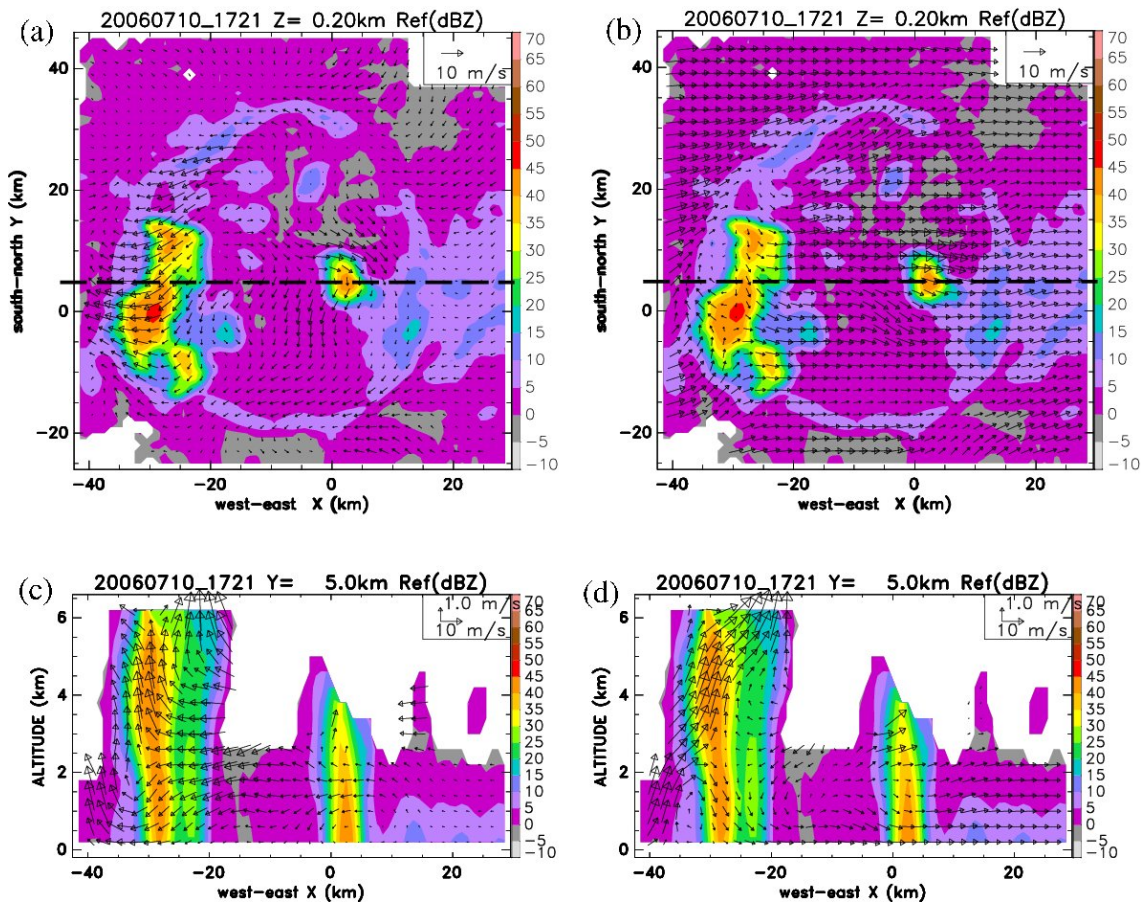


FIG. 14. Horizontal (top) and vertical (bottom) cross section of the absolute wind (left) and system-relative wind (right) obtained with MUSCAT analysis, superimposed on reflectivity and representative of the half hour centered at 1720 UTC. Horizontal dashed line in the top panels indicate the position of the vertical cross section shown in bottom panels.

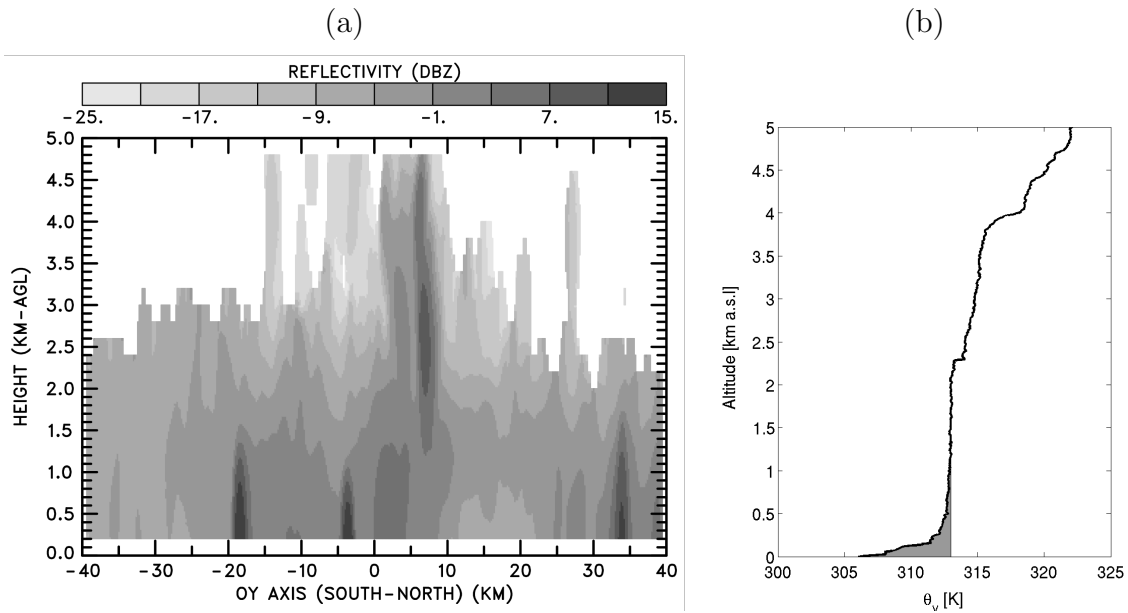


FIG. 15. (a) Vertical cross section of the reflectivity at $X = -7$ km at 1720 UTC. (b) Vertical profile of the virtual potential temperature at 1730 UTC. The WAPE is represented by the shaded surface. The edge of the wake is visible in (a) with the local maximum of reflectivity at $Y = -18$ and $Y = 34$ km, extending from the ground to about 1.5 km a.g.l.